NATIONAL TECHNICAL UNIVERSITY OF ATHENS

POSTGRADUATE STUDIES PROGRAM

"COMPUTATIONAL MECHANICS"

THESIS

Optimization of bubbler design in metalorganic chemical vapor deposition processes

By:

Georgia SAKELLARI

Supervisors:

Prof. Andreas G.BOUDOUVIS

School of Chemical Engineering NTUA

Dr. Harald LAUX

Osram Opto Semiconductors

September 2012

Περίληψη

Η παρούσα μεταπτυχιακή διατριβή εκπονήθηκε σε στενή και συνεχή συνεργασία με την OSRAM Opto Semiconductors στο Ρεγκενσμπουρκ της Γερμανίας και είχε ως σκοπό την βελτιστοποίηση διάταξης παραγωγής φυσσαλίδων - bubbler. Προς την κατεύθυνση αυτή χρησιμοποιήθηκε το λογισμικό υπολογιστικής ρευστομηχανικής ANSYS FLUENT όπου προσομοιώθηκαν οι διεργασίες εξάτμισης και συμπύκνωσης με την μέθοδο Volume Of Fluid (VOF). Επιλύθηκαν οι εξισώσεις φαινομένων μεταφοράς με κατάλληλους όρους πηγής εφαρμοζόμενους στην διεπιφάνεια των δύο φάσεων (υγρής-αέριας). Το μοντέλο επικυρώθηκε με την εφαρμογή του στο πρόβλημα Stefan, γνωστής αναλυτικής λύσης. Η βελτιστοποίηση της διάταξης περιλαμβάνει την εξέταση διαφορετικών γεωμετριών σε συνδυασμό με διαφορετικές τιμές ρυθμού ροής εισόδου, και στάθμης υγρού μέσα στον bubbler. Τα βασικά κριτήρια που χρησιμοποιήθηκαν για την ανάλυση των περιπτώσεων που εξετάστηκαν συνδέονται με τα ακόλουθα μεγέθη: το μέσο γραμμομοριακό κλάσμα του ατμού στον όγκο του αερίου και στην έξοδο, ο χρόνος παραμονής συσχετιζόμενος με την ποσότητα του αερίου που υπάρχει μέσα στο υγρό (gas hold up) και προκαλεί άνοδο της στάθμης του υγρού μέσα στον bubbler και την μέση τιμή της θερμοκρασίας σε ολόκληρη την διάταξη.

Τα βασικά συμπεράσματα της εργασίας είναι τα εξής:

- Η παρατηρούμενη συμπύκνωση στον σωλήνα τροφοδοσίας επηρεάζει την τιμή εξόδου του κλάσματος ατμού, η οποία ταυτίζεται με αυτήν της τιμής της ισορροπίας στην έξοδο του bubbler .
- Ο αυξανόμενος ρυθμός εισόδου τροφοδοσίας δεν επηρεάζει το κλάσμα ατμού στην έξοδο, όπου επιτυγχάνεται σταθερή ένδειξη, η οποία είναι σε ικανοποιητική συμφωνία με τις πειραματικές μετρήσεις.
- Η διάταξη bubbler μεγαλύτερης διαμέτρου παρουσιάζει τα επιθυμητά χαρακτηριστικά όσον αφορά την τιμή του κλάσματος ατμού (τιμή ισορροπίας) και τον χρόνο παραμονής (μεγάλο). Ωστόσο, στην διάταξη αυτή χρησιμοποιείται μεγαλύτερος όγκος υγρού (Trimethylgallium, TMG) το οποίο είναι ακριβό και επιβαρύνει το κόστος χρήσης.
- Η διάταξη bubbler μικρότερου ύψους μειώνει το μέσο κλάσμα ατμού στον όγκο του αερίου και στην έξοδο και μειώνει τον χρόνο παραμονής του αερίου στον όγκο του υγρού.

- Η διάταξη bubbler η οποία παρουσιάζει τα καλύτερα τεχνικά χαρακτηριστικά είναι αυτή όπου προστίθεται μια νέα σειρά πτερυγίων και κλείνεται μια οπή στην πλάκα διανομής του αερίου καθώς αυτό εισέρχεται και διανέμεται στον όγκο του υγρού. Η διάταξη αυτή συνδυάζει την τιμή ισορροπίας για το κλάσμα ατμού με τον μεγάλο χρόνο παραμονής καθώς επίσης διατηρεί σταθερό το κόστος του χρησιμοποιούμενου υγρού TMG.

Abstract

In this computational study, the optimization of a bubbler design, including evaporation and condensation processes, were investigated using the Volume-Of-Fluid model (VOF) in the ANSYS FLUENT code. Mass transfer contributions were calculated and source terms at the interface were accordingly incorporated in the continuity, energy and species equations. The model was validated by Stefan's problem. Different geometries in combination with different values of inlet flow rates and liquid filling degrees were studied. The main optimization criteria used to analyze the results were the average vapor mole fraction in the gas and at the outlet, the residence time associated with the gas hold up and the average temperature in the flow domain. The key findings of this work are the following:

- Reaching equilibrium at the bubbler outlet is significantly affected by the condensation at the feed pipe during the filling process
- Even at high inlet flow rates, a constant source flow is generated at the outlet, in accordance with the experimental results
- Wider bubblers are advantageous since they yield average mole fraction closer to equilibrium and higher residence time. However, they imply storage of an expensive liquid (such as Trimethylgallium, TMG)
- Reducing bubbler height increases average mole fraction in the gas and at the outlet, and reduces residence time
- Modified bubblers with an addition of internals and closing a particular hole close to the feed pipe brings the system faster to equilibrium and increases the residence time. This design comes out to be the optimum in the range of the examined design modifications

Acknowledgements

First and foremost I would like to thank my supervisor at NTUA Prof. Andreas Boudouvis for his support throughout this project.

I must give my respectful gratitude to my supervisor at OSRAM Opto Semiconductors, Dr. Harald Laux for his guidance, supervision, and help throughout this project. I have learned a lot throughout this semester, with many challenging valuable experiences in order to complete this task.

I would like to thank all the colleagues at OSRAM Opto Semiconductors especially those from the Modeling group for their daily support and help. Many thanks to Andreas Koller that designed the bubbler system for the cooperation and help. I am also thankful to Thomas Bleicher for the continued technical support he offered me.

Special thanks also to Dr. Nikolaos Cheimarios for his help with multiphase modeling and UDF programming.

I also wish to thank Socrates Garnelis for his assistance with the usage of the computational cluster at NTUA.

Last but not least, special thanks go to all of those who contributed to this work in any way.

Contents

Part I

Introduction

Chapter 1

Introduction and Literature Review

1.1 Company profile of OSRAM Opto Semiconductors

This work was carried out at OSRAM Opto Semiconductors. OSRAM Opto Semiconductors is one of the world's leading manufacturers of optoelectronic semiconductors. OSRAM produces high brightness and high power LED's. LED's include an epitaxial grown crystal with a light producing internal layer while, crystals are grown on substrates (wafers) in MOCVD reactors at OSRAM.

With its headquarters in Regensburg (Germany), Sunnyvale (USA) and in Hong Kong, production sites in Regensburg and Penang (Malaysia) and a global network of sales and marketing centers, OSRAM Opto Semiconductors is in an excellent position to meet the challenges faced by a global high-tech company [1].

1.2 Metalorganic Chemical Vapor Deposition (MOCVD)

Metalorganic chemical vapor deposition is an epitaxial deposition technology used to produce high quality electronic and optoelectronic devices. In the semiconductor industry, laser diodes, light-emitting diodes, transistrors etc. are produced. In the MOCVD process the goal is to produce solid thin films in a controlled way. Gaseous chemical precursors, pass over a heated crystalline substrate seed crystal, where pyrolytic reactions cause chemical decomposition and subsequently produce solid films.

The MOCVD equipment consists of three main parts (Fig. 1.2, [2]):

1. Chemical vapour precursor system
2. MOCVD reactor
3. Effluent gas handling system

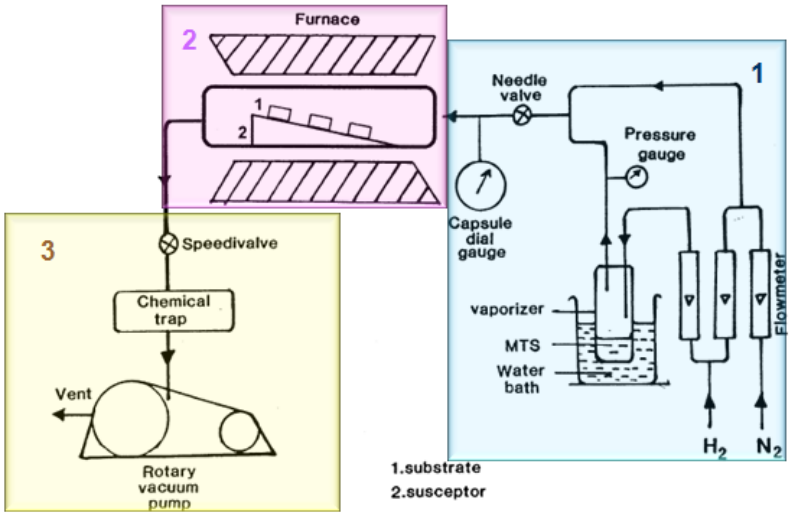

Figure 1.2: Typical laboratory MOCVD equipment for the deposition of epitaxial films on heated substrates.

In detail the main parts are as follows:

Chemical vapour precursor supply system (Fig. 1.2, 1)

The role of this part is to generate vapour precursors (solid, liquid, gas) and then deliver them to the reactor. Liquid sources use a bubbler to vaporize the reactants and a carrier gas (reactive gases as H_2 or inert gases such as N_2) to transport the vaporized reactants into the reactor. The delivery of the reactants depends on the source temperature, the carrier gas flow rate and the pressure over the source.

MOCVD reactor (Fig. 1.2, 2)

The MOCVD reactor consists of a reaction chamber equipped with a loadlock for the transport and placement of the substrate into the chamber, a substrate holder, and a heating system with temperature control. The main part of the MOCVD reactor is used

to heat the substrate to the deposition temperature. There are different types of reactors: horizontal, vertical, semi-pancake, barrel and multiple wafer [2].

The effluent gas handling system (Fig. 1.2, 3)

This part consists of a neutralizing part for the exhausted gases, and/or a vacuum system to provide the required reduced pressure for the MOCVD process that performs at low pressure or high vacuum during deposition. The main part of the effluent gas handling system is the removal of the hazardous by-products and the toxic unreacted precursor safely.

Main steps of MOCVD process

In general the main steps of the MOCVD process are [2]:

1. Active gaseous reactant species are generated
2. Gaseous species are transported into the reaction chamber
3. Gaseous reactants are forming intermediate species by reacting in the gas phase
4. Absorption of gaseous reactants onto the heated substrate where heterogenous reaction occurs at the gas-solid interface which produces the deposit and by-product species
5. Diffusion along the heated substrate surface forming the crystallisation centre and growth of the film
6. Removal of gaseous by-product from the boundary layer through diffusion or convection
7. Transportation of unreacted gaseous precursors and by-products away from the deposition chamber

Bubbler system and chemical precursors

The precursors used in a MOCVD process can be liquids and solids. Such precursors are widely used and are better on physical properties and less harmful, flammable and

corrosive compared to the gaseous ones. Here are only mentioned the liquid precursor types that are used to fill the bubbler through which the carrier gas is bubbled. The bubbler is a vessel made of steel, filled with the precursor which has to be evaporated and transported in to the reaction chamber.

There are different commercial bubbler types where the liquid is mainly heated by a temperature controlled heater device and evaporates. Temperature of the liquid determines the vapor pressure in the bubbler. Due to the strong dependence of vapour pressure on temperature, current bubbler systems have problems to deliver a stable source flow when the flow rate is increasing. To deal with this, different configurations of a new bubbler design are studied in this thesis. The typical bubbler type used in the semiconductor industry is shown in Fig. 1.3.

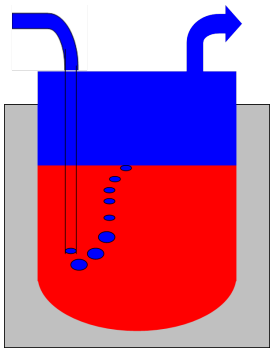

Figure 1.3: Typical bubbler type used in semiconductor industry

In the described commercial bubbler system, as the inlet flow rate increases, source flow reduces (Fig.1.5). The goal of the new design is to create a bubbler system able to conserve a stable source flow even for high inlet flow rates (above 2000 sccm).

1.3 New concept to provide stable source flow

The experimental set up consists of two bubblers connected in series. The first one (No 1 in Fig. 1.4) is a commercial bubbler like the one shown in Fig. 1.3 and is used to saturate the carrier gas before it passes through the second (No 2) in-house bubbler. The in-house bubbler is designed by OSRAM and has to be optimized. Depicted in Fig. 1.4 is a new concept of bubbler design.

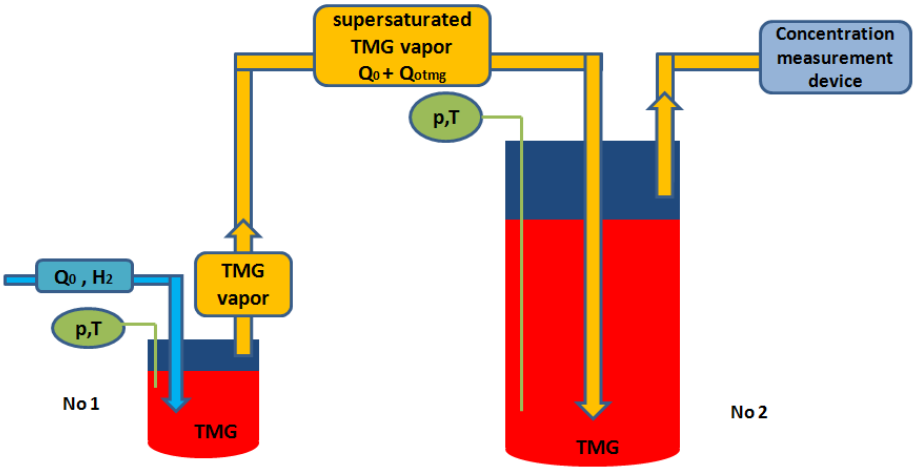

Figure 1.4: New prototype bubbler system

Pure carrier gas enters the commercial bubbler and is saturated to some degree depending on the flow rate. The vapor-gas mixture includes the carrier gas (Hydrogen gas(H_2)) with the saturated precursor (Trimethylgallium vapor $((CH_3)_3)Ga$, TMG) and enters into the second bubbler, through a centered feed pipe, which operates at a lower temperature. Therefore, the gas mixture in the second bubbler is supersaturated and vapor condensates, while it evaporates at the free surface. In this way the liquid level is kept constant in the bubbler. The mass transfer is concentration gradient driven under almost isothermal conditions. This is very important for the saturation and the delivery of the gas inside the MOCVD reactor chamber. The bubbles are distributed over the whole tank by means of a series of internals. At the outer walls water cooling is applied, to keep the bubbler on a constant temperature. The carrier gas flow, through the bubbler, is metered with an electronic MFC (mass flow controller) while the bubbler's internal pressure is controlled by an electronic BPC (back pressure controller). A concentration measurement device is

attached at the outlet.

The experimental results show that at low filling degrees the vapor mole fraction at the outlet is almost constant for different inlet flow rates even for the higher ones Fig.1.5.

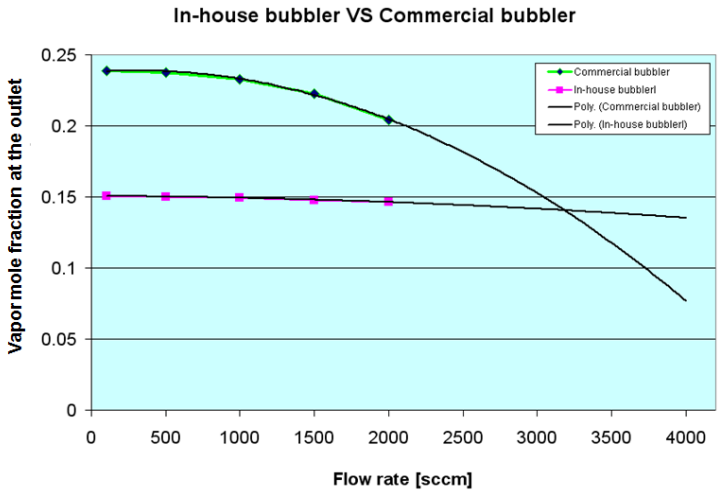

Figure 1.5: Comparison between commercial and in-house bubbler

1.4 Literature review on bubbler models

Regarding the importance of bubbler for the chemical vapor deposition processes very few theoretical, experimental and numerical work is available in the literature.

Love et al. [3] present a lumped mathematical model of the performance of a bubbler as a vapor delivery system. The model defines and elucidades the parameters that control the behavior of the bubbler and an experimental protocol was used to measure the magnitude of the thermal resistances and the response of the bubbler to changes in operating conditions.

Holstein [4] investigates the increasing partial pressure that was described in the study of Stagg et al. [5] at low flow rates by considering thermal diffusion due to temperature gradients. This increment occurs in a tube after the bubbler where the exit temperature is increased. He proposed that at low flow rates, the entire saturator should be submerged in a constant temperature bath and by using a narrow diameter extension of the exit tube in the saturator vessel. The temperature of the exit tube should be kept constant.

All the above systems are temperature sensitive and they have to be designed and

operated very carefully to ensure that the exit gas stream delivers a constant vapor pressure of the precursor.

A study from Bour [6] describes a way to calculate the filling degree in a commercial bubbler which is filled by a liquid or a solid source. Andre et al. [7] studied a prototype design of a bubbler filled by solid TMIn to overcome the issues associated with the constant delivery of a fully saturated vapor into a MOCVD reactor.

In summary, all the studies mentioned above are focusing on experimental analysis of the bubbler system along with some parametric studies regarding its operation. In this work, the bubbler is studied via a computational analysis based on Computational Fluid Dynamics (CFD).

1.5 CFD simulation of bubbler flow

Being a multiphase system, the bubbler is considered as comprising continuous and dispersed phases which can include different chemical components. The continuous phases can be liquids and/or gases. The dispersed phases can be liquid droplets, gas bubbles or solid particles depending on the continuous phase. In the particular bubbler, the flow is a two-phase one. The continuous phase is the liquid phase and the dispersed phase is the gas phase (bubbles).

There are two modeling strategies to approach multiphase systems by means of CFD:

- Free surface flow models
- The two-fluid model

Choosing a multiphase model

To solve a multiphase problem, as the bubbler flow, the choice of the appropriate model is required. **In the current study the Volume Of Fluid (VOF) model is used.** The size of the formed bubbles, is bigger compared to the mesh size and can be represented on the mesh. So, for rather low flow rates and laminar flow the VOF model can be applied.

The two-fluid model - Eulerian model

The Eulerian model treats the different phases as interpenetrating phases. It solves momentum and continuity equations for each phase. Pressure and interphase coefficients combined with the phase types are used for coupling. It is used when interfaces cannot be represented on a mesh. Typically, for vapor high flow rates and turbulent flow the dispersed bubbles that appear cannot be shown on the mesh.

The free surface flow model

The VOF model is used for tracking the interface between different continuous and immiscible fluids. Two or more fluids can be used and the equations being solved are shared by the phases and include a single set of momentum equations. The volume fraction of each phase is tracked. This model is used when interfaces are large enough (e.g. bubble-liq) to be represented on the mesh.

1.6 Purpose

The purpose of the current study is to optimize the design of the bubbler (OSRAM inhouse) by means of CFD modeling and to suggest design optimizations. The main idea is to improve the creation of fully saturated bubbles that transfer the metalorganic precursor into the MOCVD reaction chamber at constant source flow and temperature. To succeed that, more interfacial area and higher bubble residence times are probably needed. Different design parameters are varied such as the height of the bubbler, the diameter, the shape, the number and the position of the internals.

Part II

Numerical Procedure

Chapter 2

Mathematical Formulation

2.1 Governing equations

2.1.1 General Description of the model

In the current study a numerical analysis has been performed to optimize the design of a new bubbler. For this purpose a free surface model is used to model the two-phase flow and is supplied by coupled mass and heat transfer models to account for the evaporation and condensation of the liquid or vapor. Here, mass transfer is driven by the species mass fraction gradient at the gas-liquid interface and liquid evaporates to gas and gas condensates to liquid depending on the local conditions at the interface. The gas phase is defined by two species components, the precursor and the carrier gas, and the mass fraction distribution of the two species is computed. Heat transfer due to evaporation/condensation is computed as well.

A transient problem is defined, the VOF method is used and the governing equations are solved for gas and liquid phases.

2.1.2 Multiphase model

In this study the VOF method available in the commercial CFD code ANSYS FLUENT 14 is used. The VOF method is a fixed mesh technique which can model two or more immiscible fluids [8].

In the VOF model, a single momentum equation, the continuity equation and a volume fraction equation for the secondary phase are solved. Interface tracking is based on the volume fraction field of the secondary phase. In this study the gas phase is taken as secondary phase.

2.1.2.1 Volume fraction and continuity equation

The continuity equation is given by:

$$\frac{\partial \rho}{\partial t} + \nabla \cdot \rho \vec{u} = 0, \tag{2.1}$$

where, ρ $[kg/m^3]$ is the mixture density, defined below and $\vec{u}$ [m/s] is the velocity.

The equation for the gas phase volume fraction is:

$$\frac{\partial \alpha_g \rho_g}{\partial t} + \nabla \cdot (\alpha_g \rho_g \vec{u}) = S_{\alpha_g}, \tag{2.2}$$

where index g denotes gas phase variables, S_{α_g} is a source term due to mass transfer, to be defined later and α_g is the volume fraction given by:

$$\alpha_g = \frac{\text{volume of gas in a cell}}{\text{volume of the cell}}. \tag{2.3}$$

The volume fraction α_g can have the following values:

- $\alpha_g = 1$, cell is full of gas
- $\alpha_g = 0$, cell is full of liquid
- $0 < \alpha_g < 1$ if the cell is partially filled with gas and contains an interface between gas and liquid phases

The volume fraction of all phases in each control volume sums to unity. As it is considered to be a two-phase problem, the volume fraction of the liquid for the given system and for every cell is calculated by:

$$\alpha_g + \alpha_l = 1, \tag{2.4}$$

where index l denotes liquid phase variables.

The properties and the fields for all variables that appear in the conservation equations are determined from the volume fraction of each phase. For instance, density and viscosity $\mu[Pas]$, in each cell are determined by:

$$\rho = \alpha_g \rho_g + (1 - \alpha_g)\rho_l, \tag{2.5}$$

$$\mu = \alpha_g \mu_g + (1 - \alpha_g)\mu_l, \tag{2.6}$$

respectively.

In conclusion, the VOF method solves only N-1 volume fraction equations. It also uses the continuity equation to construct the pressure-correction equation for the velocity field [9].

2.1.2.2 Interface reconstruction

ANSYS FLUENT offers different methods to solve the volume fractions as the donor-acceptor method, the simple line interface calculation (SLIC) method and the piece-wise linear interface calculation (PLIC) method generalised to be used with unstructured meshes which is also called the geo-reconstruction scheme. The geo-reconstruction scheme is used in the current study as it is recommended for this type of problems. This method is illustrated in the Fig. 2.1 (b) [10]. The interface reconstruction is very important for the solution accuracy because the interfacial area is involved in heat and mass transfer.

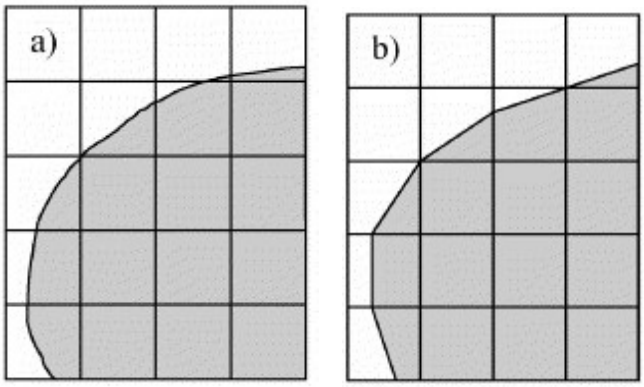

(a) Real interface shape (b) Shape calculated by VOF geo-reconstruction scheme

Figure 2.1: Geo-reconstruction scheme

2.1.3 Momentum equation

A single set of momentum equations is solved throughout the flow domain to describe the momentum transport in both phases.

The momentum equation includes the volume fractions of all phases through the properties ρ and μ:

$$\frac{\partial(\rho\vec{u})}{\partial t} + \nabla\cdot(\rho\vec{u}\vec{u}) = -\nabla p + \nabla\cdot\mu(\nabla\vec{u} + (\nabla\vec{u})^T) + \rho\vec{g} + \vec{F}. \tag{2.7}$$

In the momentum equation, accumulation and convective terms are balanced in every cell with pressure p [Pa], shear, gravitational body forces, and additional forces $\vec{F}$. Here, $\vec{F}$ is a force due to surface tension at the interface.

The surface tension force can be expressed as proposed by Brackbill et al. [11] employing the Continuum Surface Force (CSF) model:

$$\vec{F} = -\sigma_{gl}\frac{\rho\kappa_g\nabla\alpha_g}{\frac{1}{2}(\rho_g+\rho_l)}, \tag{2.8}$$

where, $\nabla\alpha_g$ is the gradient of the volume fraction in the gas phase, σ is the surface tension $[N/m]$, ρ, ρ_l, ρ_g are the mixture, liquid and gas density $[kg/m^3]$, respectively and κ_g [1/m] is the curvature.

The surface tension source term $\vec{F}$ $[N/m^3]$ in Equation 2.8 written as a pressure jump

at the interface for a two-phase system, is expressed as volume force by the use of the divergence theorem. In that way the surface tension is changed to a volume force and is added to the momentum equation.

In the simple case where surface tension remains constant and only the interfacial forces are considered, the surface tension is associated with the pressure drop across the interface and the surface curvature by the Young-Laplace equation:

$$p_2 - p_1 = \sigma(\frac{1}{R_1} + \frac{1}{R_2}). \tag{2.9}$$

where R_1 and R_2 are the radius of curvature, as shown in Figure 2.2. Thus,

$$\kappa_g = \pm(\frac{1}{R_1} + \frac{1}{R_2}), \tag{2.10}$$

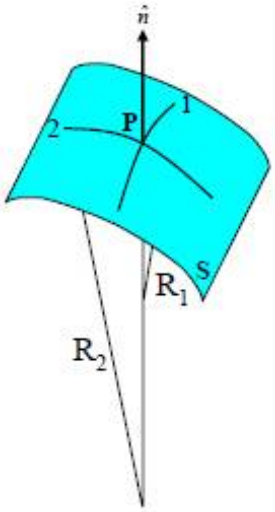

Figure 2.2: Young-Laplace equation quantities

In the general case, the curvature is computed from the surface divergence of the unit vector normal to the interface, $\vec{n}_g$:

$$\vec{n}_g = \frac{\nabla \alpha_g}{|\nabla \alpha_g|}. \tag{2.11}$$

$$\kappa_g = \nabla \cdot \vec{n}_g, \tag{2.12}$$

where, $||$ denotes the modulus of a vector.

Additionally, due to the presence of solid boundaries, in cells close to walls the interface shape is adjusted to enforce the given contact angle (θ) at the wall (Fig. 2.3). The unit normal vector in these cells is set to:

$$\vec{n} = \vec{n}_w cos\theta_w + \vec{t}_w sin\theta_w, \tag{2.13}$$

where $\vec{n}_w$ and $\vec{t}_w$ are unit vectors normal and tangential to the wall respectively.

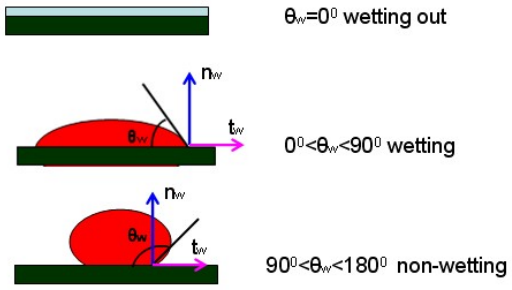

Figure 2.3: Contact angle

2.1.4 Energy equation

The energy equation is written in enthalpy form and shared between the phases:

$$\frac{\partial(\rho h)}{\partial t} + \nabla \cdot (\rho h \vec{u}) = \nabla \cdot (k\nabla T - \sum_{i=1}^{n} h_g^i \vec{J}_g^i) + S_E, \tag{2.14}$$

where, i is the index for species and n is number of species. The thermal conductivity k [W/mK] is calculated as density in Eq. 2.5 and enthalpy h [J/kg] is a mass average variable defined as:

$$h = \frac{\alpha_g \rho_g h_g + (1-\alpha_g)\rho_l h_l}{\alpha_g \rho_g + (1-\alpha_g)\rho_l}. \tag{2.15}$$

The enthalpy depends on temperature and heat capacity, C_p [J/kgK]. The temperature is calculated from:

$$h = h_0 + \int_{T_0}^{T} C_p \mathrm{d}T \tag{2.16}$$

where, T_0 [K], h_0 [J/kg] are reference temperature and enthalpy respectively. C_p is calculated as e.g. density in Eq. 2.5

The second term on the right hand side describes the enthalpy transport due to species diffusion and S_E is the source term for heat transfer related to mass transfer at the interface.

Dissipation effects (e.g. viscous) are neglected.

2.1.5 Species equation

The species equation is phase-specific and is solved only for the gas phase since here the liquid phase is not a mixture but a pure liquid:

$$\frac{\partial(\rho_g \alpha_g Y_g^i)}{\partial t} + \nabla \cdot (\rho_g \alpha_g \vec{u} Y_g^i) = -\nabla \cdot (\alpha_g \vec{J_g^i}) + S_{sp}^i, \tag{2.17}$$

where, Y_g^i is the mass fraction of component i, S_{sp}^i is the species source term due to interfacial mass transfer and $\vec{J_g^i}$ is the diffusion flux term of component i in gas phase. Here, the gas is a binary system and thus the diffusion flux is given by Fick's law:

$$\vec{J_g^i} = -\rho_g D_i \nabla Y_g^i, \tag{2.18}$$

where, D_i is the diffusion coefficient of species i.

The effect of thermal diffusion (Soret effect) is neglected because temperature gradients in the bubbler are too small.

2.2 Interface conditions

Mass transfer takes place from the liquid to the gas phase (evaporation) and from the gas to the liquid phase (condensation). To overcome the discontinuity at the interface between gas and liquid, jump conditions are used to couple interphase heat and mass transfer.

2.2.1 Mass transfer

In general mass transfer is coupled and driven by concentration and temperature gradients at the interface. As already mentioned, due to small temperature differences but large concentration gradients here it is assumed that the mass transfer is driven by the concentration gradients only. Assuming that A $[m^2]$ is the interfacial area in a cell with volume V_{cell} $[m^3]$, then the model used can be written as:

$$\dot{m}_i''' = \frac{\rho_g K A}{V_{cell}}(Y_g^{i*} - Y_g^i), \tag{2.19}$$

where, $\dot{m}_i'''$ is the volumetric rate $[kg/m^3 s]$, K [m/s] the overall mass transfer coefficient and Y_g^{i*} the mass fraction of species at the interface defined by the equilibrium value based on the vapor pressure (Eq. 2.44).

The interfacial area is given by:

$$A = V_{cell}|\nabla \alpha_g|. \tag{2.20}$$

Inserting Eq. 2.20 into Eq. 2.19 the mass transfer formulation used, is given by:

$$\dot{m}_i''' = \rho_g K(Y_g^{i*} - Y_g^i)|\nabla \alpha_g|. \tag{2.21}$$

A combined diffusive and convective mass transfer formulation for the flux $\dot{m}_i''$ $[kg/m^2 s]$, can be written as [12]:

$$\vec{\dot{m}}''_i = \vec{J}_g^i + \rho_g^i \vec{u} = \vec{J}_g^i + Y_g^{i*} \sum_{i=1}^{n} \vec{\dot{m}}_i''. \tag{2.22}$$

Since here only a single gas phase species participates in the mass transfer $\rho_g^i u = Y_g^{i*} \vec{\dot{m}}_i''$ we find [13]:

$$\dot{\vec{m}}_i'' = -\rho_g D_i \nabla Y_g^i + Y_g^{i*} \dot{\vec{m}}_i'', \tag{2.23}$$

and:

$$\dot{m}''' = \dot{\vec{m}}'' \frac{\vec{A}}{V_{cell}} = \dot{\vec{m}}'' \cdot \nabla \alpha_g, \tag{2.24}$$

thus:

$$\dot{m}''' = -\frac{\rho_g D_i}{1 - Y_g^{i*}} \nabla Y_g^i \cdot \nabla \alpha_g, \tag{2.25}$$

The overall mass transfer coefficient approximation is obtained by the comparison of Eq. 2.21 with Eq. 2.25 :

$$\rho_g K (Y_g^{i*} - Y_g^i) |\nabla \alpha_g| = \frac{-\rho_g D_i}{1 - Y_g^i} \nabla Y_g^i \cdot \nabla \alpha_g. \tag{2.26}$$

If ∇Y_g^i is approximated as $\frac{(Y_g^i - Y_g^{i*})}{L}$, where L is an appropriate length scale, and $\nabla \alpha_g$ as $|\nabla \alpha_g|$, then the overall mass transfer coefficient is given by:

$$K = \frac{D_i}{1 - Y_g^{i*}} \frac{1}{L}, \tag{2.27}$$

and is validated later.

In the bubbler system the length scale is chosen $L = V_{cell}^{1/3}$.

The final form of the used mass transfer model is:

$$\dot{m}_i''' = \rho_g \frac{D_i}{1 - Y_g^{i*}} \frac{1}{L} (Y_g^{i*} - Y_g^i) |\nabla \alpha_g|. \tag{2.28}$$

2.2.1.1 Mass related source terms

Appropriate volumetric sources for evaporation and condensation and related heat transfer have to be added to the governing equations because such terms are not available by default in the ANSYS FLUENT VOF model. The units of the source terms for continuity and species equations are $\frac{kg}{m^3 s}$ and of the energy source term is $\frac{J}{m^3 s}$. Figure 2.4 illustrates the position of the needed source terms in a given bubble.

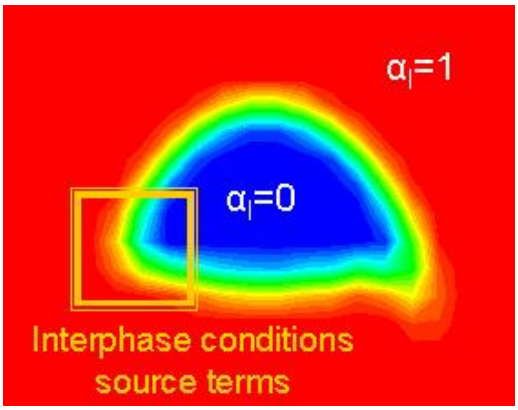

Figure 2.4: Interphase mass transfer in a bubble

Volumetric species sources - species equation

In the species equation the source term is added to model mass transfer at the interface between liquid and vapor.

It is added to the vapor species equation only:

$$S_{sp}^{vap} = \dot{m}_{vap}^{'''}. \tag{2.29}$$

Positive source terms model evaporation and negative condensation.

The source term for the gas phase continuity equation is given by the sum of the source terms for the species equations. Regarding that there is zero source term for the carrier gas only the species source for the vapor precursor exist and satisfies the desired balance equation.

Volumetric mass sources - VOF equation

Liquid and gas phase mass sources related to the species source are:

$$S_l = -S_{sp}^{vap}, \tag{2.30}$$

$$S_g = S_{sp}^{vap}, \tag{2.31}$$

respectively. Thus, in case of evaporation, $S_{sp}^{vap} > 0$, liquid is consumed and for condensation liquid is created.

The overall continuity equation, (Eq. 2.1), should be satisfied and the sum of the source terms S_l and S_g should be zero: $S_l + S_g = -S_{sp}^{vap} + S_{sp}^{vap} = 0$.

Volumetric energy sources - Energy equation

The energy source is calculated from the species source and the latent heat by:

$$S_E = -S_{sp}^{vap} \Delta H_{vap}, \tag{2.32}$$

where, ΔH_{vap} is the latent heat in J/kg and is always positive. In case of evaporation $S_{sp}^{vap} > 0$ and the gas/liquid mixture is cooled, while for condensation it is heated.

Momentum equation

In the single momentum equation the source term is zero because the momentum source terms in the liquid and gas should balance.

2.2.1.2 Numerical implementation

Numerical problems were encountered which could be remedied using the following stabilization means.

In this study Eq. 2.28 is multiplied by the factor $2\alpha_l$ recommended by Banerjee [14]. By definition the interface is located where the volume fraction is equal to 0.5, although, the interface in the VOF method is smeared over a few cells as shown in the Fig. 2.5. Considered a region at the interface where, liquid (right side) exceeds the value of 0.5 and gas (left side) with values lower than 0.5, where evaporation takes place from liquid to gas. Then $2\alpha_l$ never exceeds 1, because the mass transfer term is only calculated on

the gas side of the interface. Thus, the factor is 1 at the interface and much smaller elsewhere. It was checked that this modification introduces only a small error but improves the computational stability considerably.

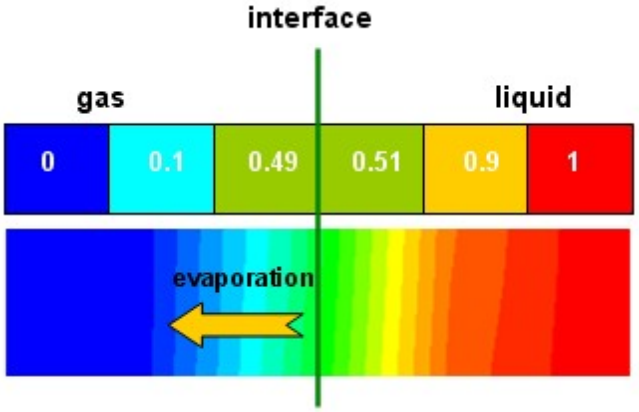

Figure 2.5: Definition of the stability term

Other implementations to improve the stability of the mass transfer model is the multiplication with factors such that cells with very low gas volume fractions and/or interfacial area do not exchange any mass. The factors are designed to give a smooth transition between the low and higher values.

The models used are the following:

Volume fraction limit

The driving force for the mass transfer according to Eq. 2.28 is $(Y_g^{i*} - Y_g^i)$. It is reformulated as, driving force $= (Y - Y_g^i)$, where Y is a function given by:

$$Y = Y_g^{*i}\phi + Y_g^i(1-\phi), \tag{2.33}$$

where ϕ is a factor dependent on the volume fraction in the following way:

- if $\alpha_g < \alpha_{g_{low}}$, $\phi = 0$, $Y = Y_g^i$, no mass transfer occurs.
- if $\alpha_{g_{low}} < \alpha_g < \alpha_{g_{high}}$,

$$\phi_\alpha = exp[\frac{-15}{(1-\frac{\alpha_{glow}}{\alpha_{ghigh}})}/(1-\frac{\alpha_g}{\alpha_{ghigh}})], \tag{2.34}$$

- if $\alpha_g > \alpha_{g_{high}}$, $\phi = 1, Y = Y_g^{i*}$, full mass transfer according to Eq. 2.28

Limit of $\beta = |\nabla \alpha_g|$ ***in Eq. 2.28***

The term β is reformulated as:

$$\beta = |\nabla \alpha_g| \phi_\alpha \tag{2.35}$$

where ϕ_α is a dimensionless factor, calculated as follows:

- if $|\nabla \alpha_g| < \beta_{low}, \phi_\alpha = 0, \beta = 0$,
- if $\beta_{low} < |\nabla \alpha_g| < \beta_{high}$,

$$\phi = exp[\frac{-15}{1 - \frac{\beta_{low}}{\beta_{high}}} / (1 - \frac{|\nabla \alpha_g|}{\beta_{high}})], \beta = f(\phi_\alpha), \tag{2.36}$$

- if $|\nabla \alpha_g| > \beta_{high}, \phi_\alpha = 1, \beta = |\nabla \alpha_g|$

Values used for the limis were $\alpha_{glow} = 0.025$, $\alpha_{ghigh} = 0.075$, $\beta_{low} = 0.1$, $\beta_{high} = 2$ which are all small compared to typical values close to interfaces.

2.3 Solution method

A control-volume-based technique is used by ANSYS FLUENT 14 to convert the governing equations into algebraic equations that can be solved numerically. To model the source terms, User Defined Functions (UDF) are used. The UDF is a routine programmed by the user written in the C programming language and FLUENT macros and is dynamically linked to the solver. Pressure-velocity coupling is achieved by using the Pressure-Implicit with Splitting Operators scheme (PISO) [15]. The continuity equation was spatially discretized by the Pressure Staggering Option (PRESTO!). The momentum, energy and species equations were discretized by a Second Order Upwind scheme. Additionally, the Geo-Reconstruction interpolation scheme (generalized PLIC approach) was used for interface tracking. The volume fraction equation was solved by an explicit scheme. Adaptive time stepping was used and the time step is adjusted to maintain a CFL number ($CFL = \frac{u_{max}\delta t}{\delta x}$) of 0.25 because the time-accurate behavior of the VOF solution is important [16].

In conclusion, Table 2.1 summarizes the used numerical schemes/settings.

Computational parameter	Settings
Solver	Pressure based transient
Discretization	Pressure (PRESTO!)
	Momentum (Second Order Upwind)
	Volume fraction (Geo-reconstruct)
Pressure-velocity coupling	PISO
Transient formulation	First Order Implicit
Convergence level	$1x10^{-6}$
Time step minimum	0.0001

Table 2.1: Numerical settings

2.3.1 Physical properties

In the current study the liquid phase is liquid TMG (Trimethylgallium $Ga(CH_3)_3$). The gas phase is a mixture of a TMG vapor and hydrogen (carrier gas). The properties of the

materials used for the calculations are given by the Tables 2.2, 2.3, 2.4 and 2.7. Temperature variations are small so it is decided to assume constant properties.

Liquid TMG properties

The liquid density is provided by the supplier. Liquid viscosity is given by [17], thermal conductivity is given for a constant temperature from the ASPEN software [18] and specific heat is defined according to [19]. Antoine and Clausius Clapeyron equations are used to calculate the vapor pressure and the latent heat of vaporization for the TMG:

$$ln(\frac{p_2}{p_1}) = \frac{-\Delta H_{vap}}{R}(\frac{1}{T_2} - \frac{1}{T_1}), \tag{2.37}$$

where, ΔH_{vap} $[J/mol]$ is the latent heat, R is the gas constant $[J/molK]$ and T_1 is the operating temperature and T_2 is the inlet temperature in [K], p_1 and p_2 are the vapor pressures at the temperatures T_1 and T_2, respectively, in [Pa]. The latent heat of vaporization is always positive.

All the properties for liquid TMG are listed in Table 2.2

Properties	TMG	Temperature
density $[kg/m^3]$	1151	20^oC
viscosity $[kg/ms]$	0.0007	20^oC
specific heat $[J/kgK]$	1631	17^oC
thermal conductivity $[W/mK]$	0.11191	25^oC
latent heat $[J/kg]$	285997	$17^oC - 22^oC$
molecular weight $[kg/kmol]$	114	

Table 2.2: Physical properties of liquid phase (TMG liquid)

TMG vapor and hydrogen properties

The gas phase species are H_2 carrier gas and TMG vapor. Properties for H_2 are provided by the ANSYS FLUENT database and are listed in Table 2.3. TMG vapor density is provided by the "Air Liquide" company. Specific heat, thermal conductivity, heat capacity and viscosity are calculated according to the kinetic theory (Appendix) at the operating temperature of 17^oC.

Properties	TMG vapor	Hydrogen
density $[kg/m^3]$	4.856	0.08189
viscosity $[kg/ms]$	0.00002548	0.00000841
specific heat $[J/kgK]$	36.46	$piecewise-polynomial$
thermal conductivity $[W/mK]$	0.000931	0.1672
molecular weight $[kg/kmol]$	114	2

Table 2.3: Physical Properties TMG vapor and H_2

Gas mixture properties

The gas phase mixture properties calculated from kinetic theory and shown in Table 2.4, where typical values are presented at the operating temperature $T_{in} = 22^oC$.

Properties	Gas mixture
density $[kg/m^3]$	1.34
viscosity$[kg/ms]$	0.000009
specific heat$[J/kgK]$	900
thermal conductivity$[W/mK]$	0.068

Table 2.4: Physical properties of gas phase

Mass diffusivity was calculated using the Wilke and Lee (1955) [20] formula at the operating temperature:

$$D_{AB} = 0.0001 \frac{[3.03 - (0.98/M_{AB}^{1/2})](10^{-3})T^{3/2}}{pM_{AB}^{1/2}\sigma_{AB}^2\Omega_D}, \tag{2.38}$$

where, D_{AB} is the binary diffusion coefficient $[m^2/s]$, T is the temperature [K], M_A, M_B are the molecular weights of A and B $[g/mol]$, $M_{AB} = 2[(1/M_A) + (1/M_B)]^{-1}$ and p is the pressure in [bar], $\sigma_{AB} = (\sigma_A + \sigma_B)/2$ [Angstroms] is the characteristic Lennard-Jones length, and Ω_D is given by:

$$\Omega_D = \frac{A}{T^{*B}} + \frac{C}{exp(DT^*)} + \frac{E}{exp(FT^*)} + \frac{G}{exp(HT^*)}, \tag{2.39}$$

where $T^* = T/(\varepsilon_{AB}/\lambda)\ \lambda[J/K]$ is the Boltzmann constant and ε_{AB} is the characteristic Lennard-Jones energy, $\varepsilon_{AB} = (\varepsilon_A\varepsilon_B)^{1/2}$, and the values A, B, C, D, E, F, G, H are given

in Table 2.5:

Constant	Value
A	1.06036
B	0.15610
C	0.19300
D	0.47635
E	1.03587
F	1.52996
G	1.76474
H	3.89411

Table 2.5: Constant values

Values for the mass diffusivity that are used in the calculations refered to the operating temperatures 10^0C and 17^0C and are given in Table 2.6.

Mass diffusivity $[m^2/s]$	Temperature
0.00002717	10^0C
0.00002839	17^0C

Table 2.6: Mass diffusivity at different operating temperatures

For the density is used the so-called incompressible ideal gas approach:

$$\rho = \frac{p_{op}}{RT\sum\frac{Y_g^i}{M_{wi}}}, \tag{2.40}$$

where, R [J/K mol] is the universal gas constant and p_{op} [Pa] the operating pressure. By using this approach, density is a function of temperature and gas composition.

Further, the surface tension is calculated by the Parachor method [20], used for organic compounds for which group values are available. The formula used is:

$$\sigma = [P(\frac{c_l - c_g}{10^3})]^4 \tag{2.41}$$

where $c_l[kmol/m^3]$ and $c_g[kmol/m^3]$ are the saturated molar liquid and gas densities, respectively. P is the parachor factor for each group. In this study the Parachor factors for

methylene and gallium are 55.25 and 50 respectively and the calculated surface tension is 0.021 N/m.The contact angle used in the current study is 60^0. Note that the angle has been varied, $60^0 - 120^0$, but without noticeable effect on the solution.

Steel properties

The solid parts of the bubbler are made of steel. The properties of the steel are taken from the ANSYS FLUENT database and are listed in Table 2.7.

Properties	Steel
density $[kg/m^3]$	8030
specific heat$[J/kgK]$	502.48
thermal conductivity$[W/mK]$	16.27

Table 2.7: Physical properties of solid steel

Properties at the interface

It is assumed that the property values at the interface are given by their respective thermodynamical equilibrium values: Y_g^{tmg*}=Y_{tmg}^*. Applying Raoult and Dalton laws the equilibrium mole fraction can be calculated as (Fig.2.6):

$$x_{tmg} = \frac{p_{vap}}{p_{op}}, \tag{2.42}$$

where p_{vap} is the vapor pressure.

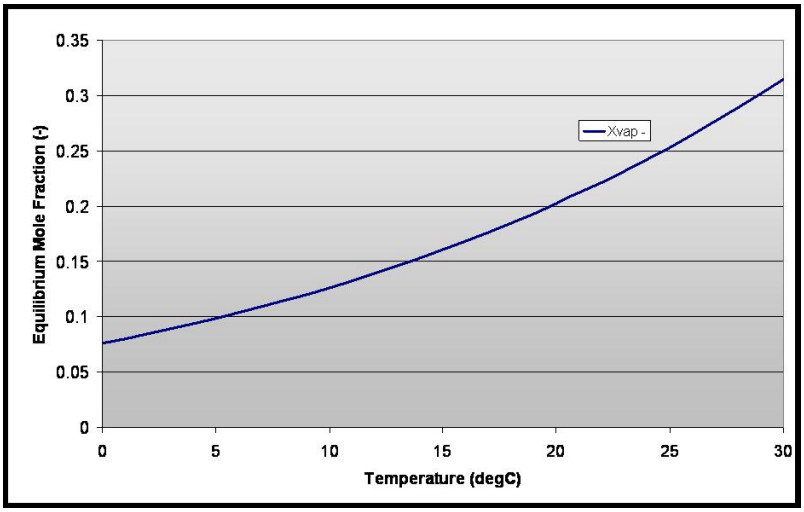

Figure 2.6: Equilibrium mole fraction of TMG

The vapor pressure for the TMG is a function of temperature (Fig. 2.7):

$$p_{vap} = 133.32 \cdot 10^{(8.07 - \frac{1703}{T})}, \tag{2.43}$$

and p_{vap} is given in $[Pa]$ and T in $[K]$.

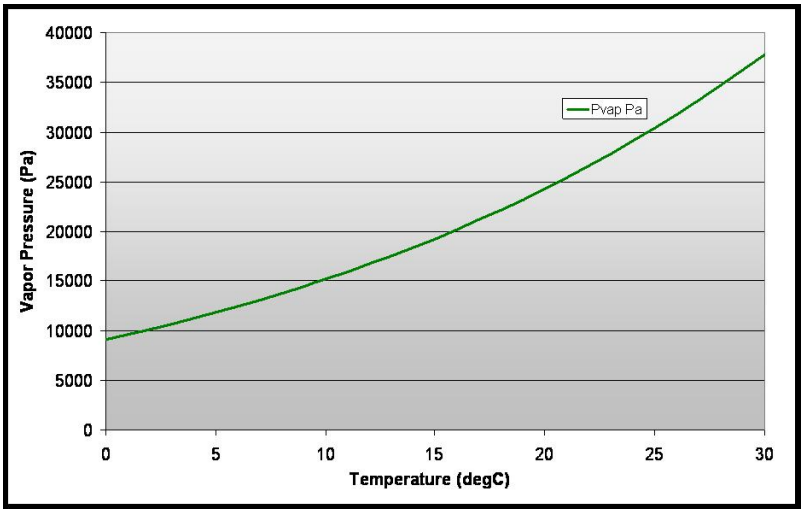

Figure 2.7: Vapor pressure of TMG as a function of temperature

Note that since the hydrostatic pressure and the dynamic pressure differences are very small (4000 Pa) compared to the operating pressure (120000 Pa), their effect on vapor concentration and gas density are negligible in this study.

The interface and equilibrium mass fraction of TMG vapor is then given by:

$$Y^*_{tmg} = \frac{x_{tmg} M_{tmg}}{x_{tmg} M_{tmg} + (1 - x_{tmg}) M_{H_2}} \tag{2.44}$$

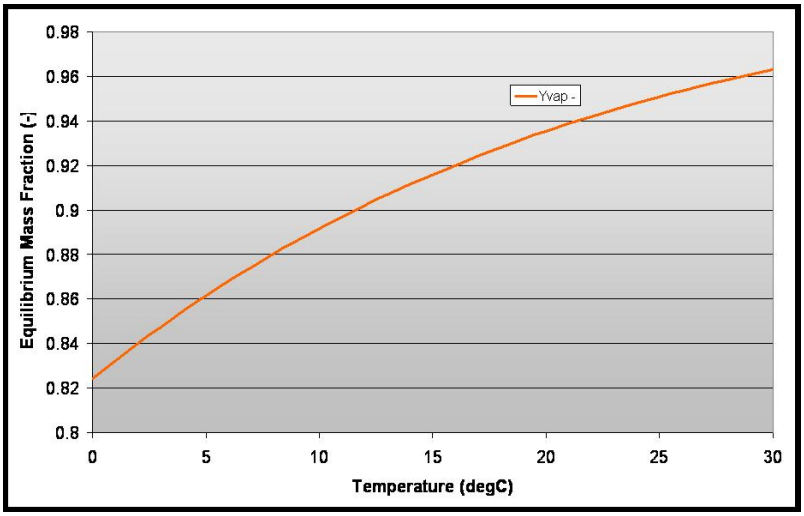

Figure 2.8: Equilibrium mass fraction of TMG

2.3.2 Validation

2.3.2.1 The Stefan problem

To validate the mass transfer source term, the Stefan problem is used [21]. The overall mass transfer coefficient (K) is defined by the Eq. 2.27.

In the Stefan problem the length scale (L) is the typical length of a cell, a constant for the used meshes.

The Stefan diffusion problem describes the evaporation of a volatile liquid from a partially filled container. In the current study, a vertical tube is partially filled with pure liquid TMG, elsewhere the tube is filled with H_2. Liquid TMG evaporates and the mole fraction distribution of TMG is determined as a function of time. Evaporation occurs at the gas-liquid interface. The species equation is solved and the problem is approximated to be 1-D by imposing zero-gradient conditions for the mass fractions at the side walls.

In the current study two models are compared. The Stefan tube analytical solution is given by calculating the species distribution in a tube where equilibrium mass fraction at the bottom and zero mass fraction at the top of the tube were imposed and only the diffusion equation is solved (Fig. 2.9 left-hand-side). The numerical solution is given by solving the mass transfer model including the source term from Eq. 2.28.

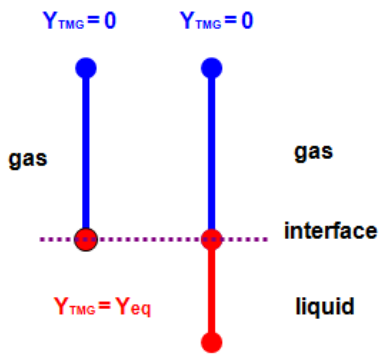

Figure 2.9: Stefan tube boundary conditions

Figure 2.10 displays the contours of the TMG mole fraction at t=150s (numerical solution).

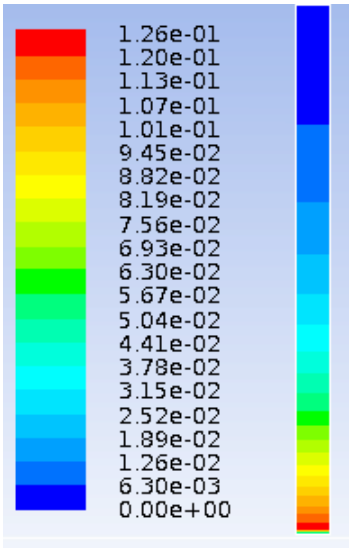

Figure 2.10: Contours of evaporating TMG mole fraction at $t = 150s$ (right column). The left column shows the colour scale.

Figure 2.11 compares the mole fraction of TMG vapour obtained from CFD and analytical solutions. It is concluded that the numerical solution is in good agreement with the analytical and as a result the mass transfer source term is an adequate basis for investigation of evaporation and condensation in the bubbler. Also, different mesh and geometry sizes were tested and the comparison was equally good.

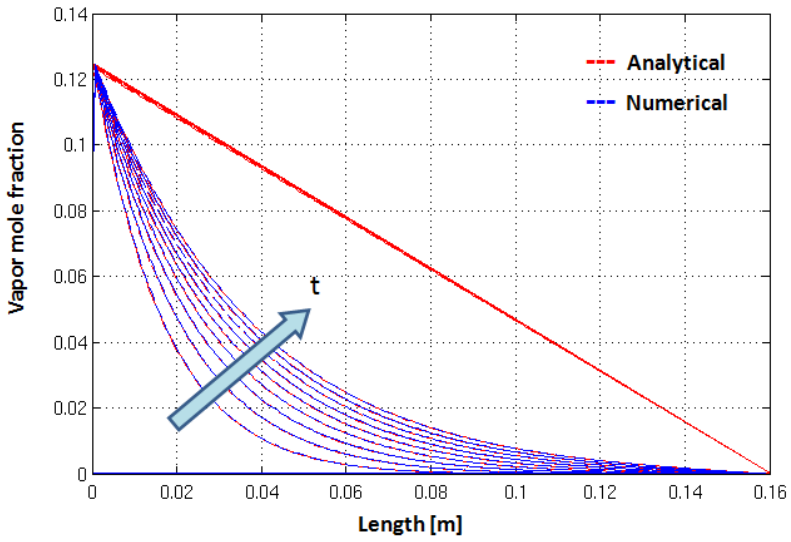

Figure 2.11: Comparison between analytical and numerical solution

2.4 Model Set-up

2.4.1 Geometry and Mesh

The geometry and the mesh were created in the ANSYS Design Modeler and are shown in Fig. 2.12. The bubbler geometry is modeled as 2D axisymmetric. The original design has a centered inlet tube, three series of internals and two perforated plates at the bottom and at the top of the bubbler. The main role of the internals and the perforated plates is to increase the residence time and the interfacial area.

The 2D axisymmetric approach can be used because the bubbler is cylindrical 3D symmetric about an axis. The modeled 2D domain represents a slice of the actual 3D model which, if revolved around the X-axis of the reference cartesian coordinate system, would become the original 3D structure.

The dimensions of the bubbler are given in the Table 2.8 where $d_{in} > d_{out}$ and $H > W$.

Dimensions	Symbol
Inlet diameter	d_{in}
Outlet diameter	d_{out}
Height	H
Width	W

Table 2.8: Dimensions of the bubbler geometry

The geometry used for the calculations is depicted in Fig. 2.12. Variations of this geometry are tested to optimize the current design.

A uniform mesh with maximum skewness of 0.79 is used. Edge sizing and inflation around the internals is applied. The mesh size used for the original geometry is 12456 nodes. Meshing influences the accuracy, convergence and speed of solution, so its role is critical for the quality of the solution. Naturally, the resolution should be as high as possible, but higher resolution costs more in computing resources. Thus, a compromise between mesh resolution and computational cost was necessary. A sample mesh used for the calculations is shown in Fig. 2.12.

Here, the focus is given to the design information that can be extracted from the sim-

ulations. By increasing the number of cells the computational time increases. The simulations in this study are transient and need long time to reach statistically steady-state conditions. A typical simulation time to reach statistically steady-state conditions with a rather coarse mesh is almost a week. Finer meshes were also checked but the design information could be extracted from the coarse one fast and reliable.

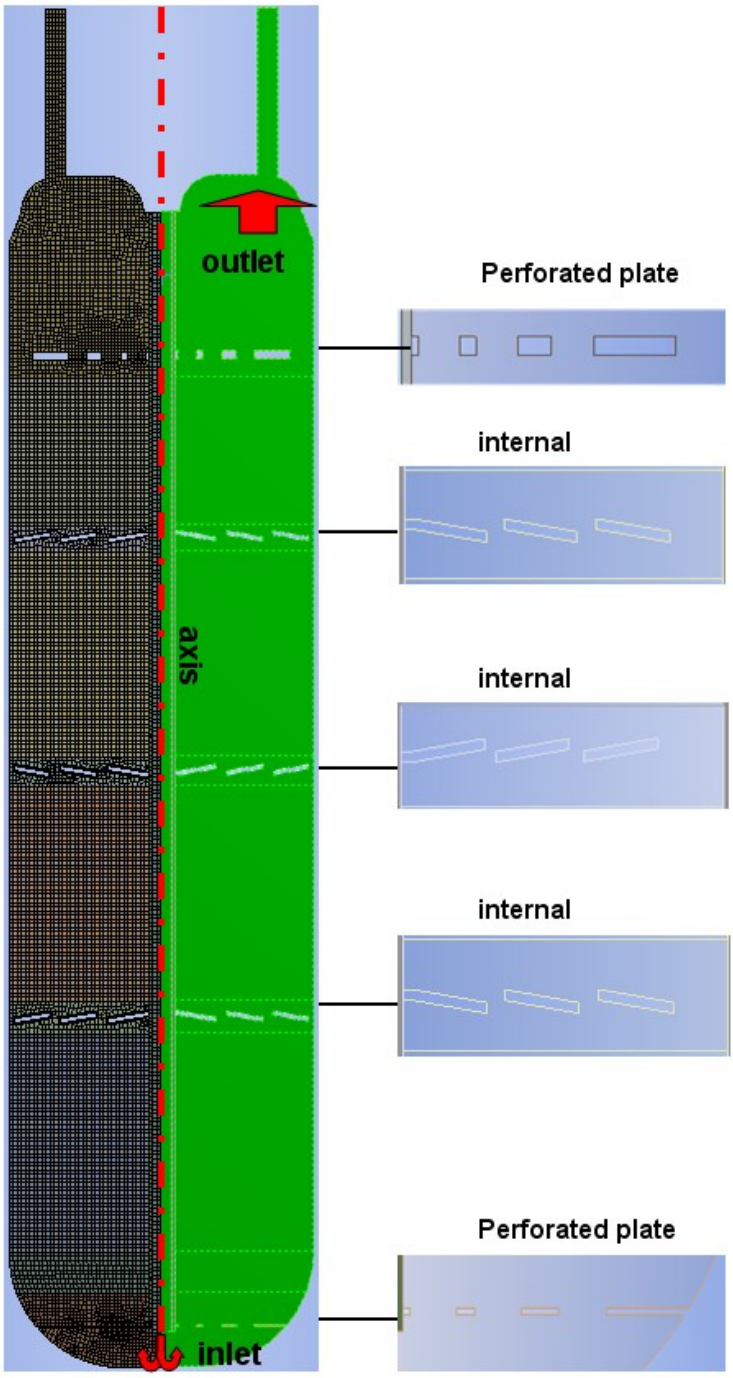

Figure 2.12: Geometry and Mesh of the initial bubbler design

2.4.2 Set up - Solution procedure

In this section initial and boundary conditions of the model are described and simplifications are justified.

2.4.2.1 Initial and Boundary conditions

The initial and the boundary conditions are depicted in the Fig. 2.13.

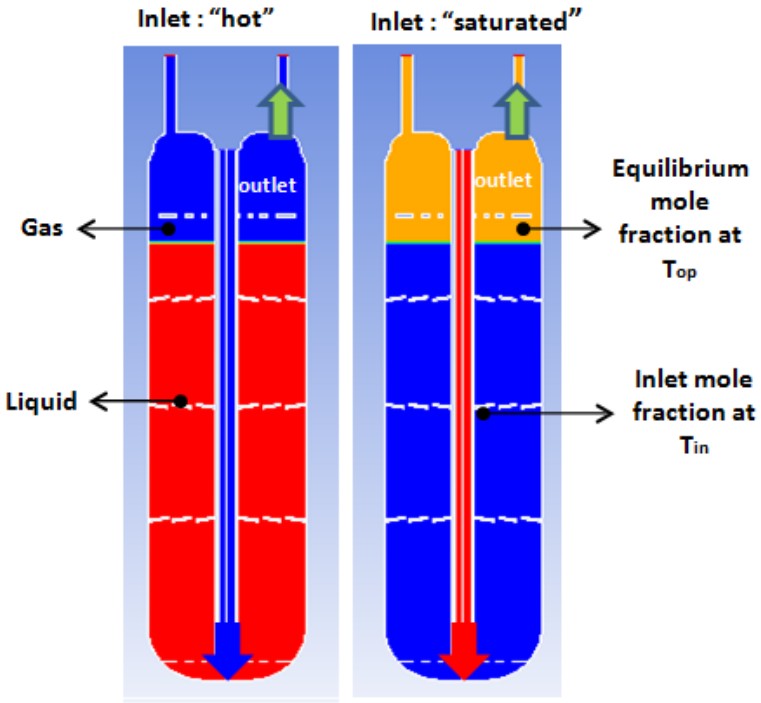

Figure 2.13: Initial and Boundary conditions

Inlet

The inlet gas is introduced at the top of the centered tube at a constant velocity, temperature and composition (Fig. 2.13). The inlet gas temperature was T_{in}. The inlet gas consists of two components, the carrier gas and the vapor precursor. Different cases of the inlet composition have been examined according to experiments and to the industrial practice. The inlet velocity is calculated from:

$$u_{in} = \frac{Q_{in}}{A_{in}} \frac{T_{in}}{T_0} \frac{p_0}{p_{op}} \tag{2.45}$$

where, $T_0 = 0\ ^oC$, $p_0 = 101325$ Pa are the Standard conditions, T_{in} the inlet temperature and p_{op} the operating pressure.

Q_{in} is the sum of the inlet flow rates of the carrier gas and the precursor (TMG) coming from the commercial bubbler Fig. 1.4:

$$Q_{in} = Q_0 + Q_{0tmg} = Q_0 + Q_0 XS \tag{2.46}$$

where, Q_0 is the inlet flow rate to the commercial bubbler, Q_{0tmg} is the flow rate of pure TMG vapor extracted from the commercial bubbler, S is the degree of saturation in the commercial bubbler and X is given by:

$$X = \frac{p_{vap}}{p_{op} - p_{vap}}. \tag{2.47}$$

The saturation degree is an approximation that comes from the experimental data (Fig. 1.5) and the value of $S = 0.9$ is used for the simulations.

Walls

The walls in the model are approximated as smooth walls and the no-slip condition is applied for the velocity and the zero-gradient condition for mass fraction. The bubbler system is adiabatic except for the heat loss by the cooling system applied to the walls. Heat transfer occurs through the walls and cooling conditions were imposed with heat transfer coefficient $h_{ex} = 15000 W/m^2 K$ and temperature $T_{ex} < T_{op}$. The contact angle at the walls was set at $\theta_w = 60^0$. In special cases condensation at the walls was modelled by setting the equilibrium mass fraction value at the wall instead of the zero-gradient condition.

Outlet

At the outlet the pressure value was imposed. Regarding temperature(operating), mass and volume fraction for bubbler-gas (equilibrium at operating temperature), appropriate "backflow conditions" were set.

Initial conditions

The initial conditions are specified in the following way. Initially, the bubbler was already partially filled and the operating temperature and pressure are T_{op}, p_{op}. Above the liquid level equilibrium mass fraction at the operating temperature and pressure are

patched. In the inlet tube inlet flow rate, bubbler-gas and mass fraction according to the saturation degree were patched.

2.4.2.2 Assumptions

Laminar flow

In the current study laminar flow is assumed. To justify this assumption, Reynolds numbers $Re = \frac{\rho u L}{\mu}$ are calculated at the inlet pipe and in the whole geometry by taking the inlet diameter and the bubbler diameter as characteristic length scales (L), respectively. Also local Reynolds numbers are calculated by tracking single bubbles in the flow domain.

Inlet pipe

The characteristic length in that case is the inlet pipe diameter, d_{in} [m]:

$$Re = \frac{\rho_g u_{in} d_{in}}{\mu_g}, \tag{2.48}$$

where, u_{in} $[m/s]$ is the inlet velocity. The table below shows the Reynolds number for different inlet flow rates and it is shown that the flow is laminar even for the highest flow rates.

Inlet flow rates [sccm]	Inlet velocity [m/s]	Reynolds number
50	0.02	21
100	0.041	42
500	0.2	212
1000	0.41	425
1500	0.61	638
2000	0.82	851
2500	1.02	1064
3000	1.23	1276
3500	1.43	1489

Table 2.9: Reynolds number as a function of inlet flow rate (velocity)

The properties used to calculate the Reynolds number are taken for the gas phase at 22^0C and for the inlet gas phase composition.

The flow in a pipe is laminar when $Re < 2300$ and turbulent when $Re > 4000$ [22].

Bubbler diameter

The Reynolds number is calculated also based on the bubbler diameter as:

$$Re = \frac{\rho_l u_{sup} d_b}{\mu_l}, \tag{2.49}$$

where, u_{sup} is the superficial velocity calculated by the area and the d_b is the bubbler diameter. The properties (ρ_l and μ_l) used to calculate the Reynolds number are for the liquid phase. Values of the Reynolds numbers are shown in Table 2.10:

Inlet flow rates [sccm]	Superficial velocity	Reynolds number
50	0.00025	25
100	0.0005	51
500	0.0025	257
1000	0.005	517
1500	0.0075	772
2000	0.01	1029
2500	0.0126	1287
3000	0.0151	1544
3500	0.0176	1802

Table 2.10: Reynolds number as a function of interfacial velocity

Single bubble

The Reynolds numbers for different single bubbles in the flow domain is calculated by Eq. 2.50 and is shown in Table 2.11.

$$Re = \frac{\rho_l u_T d_{bubble}}{\mu_l}, \tag{2.50}$$

where, u_T is the terminal velocity and d_{bubble} is the bubble diameter. The properties (ρ_l and μ_l) used to calculate the Reynolds number are for the liquid phase. Since it was

difficult to determine the terminal velocity from the simulation data, it was approximated by the rise velocity which could be measured easily in the simulation results and is much higher than the terminal. Thus, actually bubble Reynolds numbers are expected to be even smaller.

Bubble diameter [m]	Reynolds number
0.001	90
0.015	369
0.004	1951
0.0005	189

Table 2.11: Reynolds number for rising single bubbles

The Fig. 2.14 taken by Clift et al. [23] shows the wake formation around a bubble and values of the Reynolds numbers for which the wake remains steady and the flow laminar ($Re < 130$). For Reynolds numbers $130 < \mathrm{Re} < 400$ a transition range and wake instability exists. Fully unsteadiness and wake instability appear for $\mathrm{Re} > 400$.

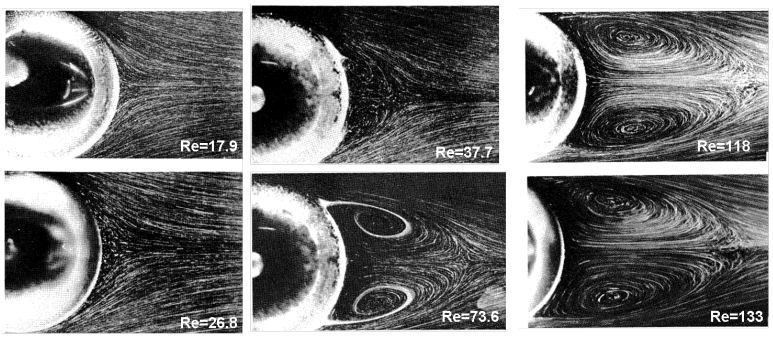

Figure 2.14: Laminar wakes around rigid spheres

The high Re values in the above table are for the largest bubbles few in number that move fast through the fluid domain thus they are not able to create much turbulence.

The above calculations justify the assumption that the flow in the bubbler is laminar. Holstein [4] assumed that the flow in a similar bubbler is laminar; the Reynolds number (up to 100) was calculated with both exit tube and bubbler diameter at low gas flow rates (0-50 sccm). Flow in the study of Love et al. [3] assumed laminar; the Reynolds numbers

did not exceed values of about 300 for flow rates up to 1000 sccm. Holstein [4] used TMG as source and Love et al. [3] used corn and syrup/water as liquid sources.

2.4.3 Computational Requirements

The numerical simulations were executed on the software platform of FLUENT 14 at OSRAM OS with a Fujitsu Celisus R570 Workstation with an Intel Xenon X5660 @2.8GHz 2x6 core processor with 48Gbyte RAM; 4 processors were used for computations. Simultaneously, they were executed on a FLUENT 6.3.26 with the high performance computing system "Pegasus" in the School of Chemical Engineering at the National Technical University of Athens (32 processors, 32Gbyte RAM) [24]. 5 processors were used for each simulation. Computer time required for a simulation up to reaching steady-state was 3 days; this was for a problem consisting of about 78000 unknowns running on the Fujitsu Celisus Workstation.

Part III

Results and Discussion

Chapter 3

Results and Discussion

3.1 Results

3.1.1 Bubble characteristics

There are two main different types of bubbles, static and in motion. The static bubbles have three different types sessile, pendant and floating and are used for determination of surface tension and contact angle. The bubbles in motion are grouped in the following categories (Fig. 3.1):

1. *spherical*: inertia forces are less important than the interfacial tension and viscous forces
2. *ellipsoidal*: formation of oblate ellipsoids with semi axes a and b
3. *spherical-cap or ellipsoidal cap*: cut spherical bubble or an ellipsoidal type with low eccentricity

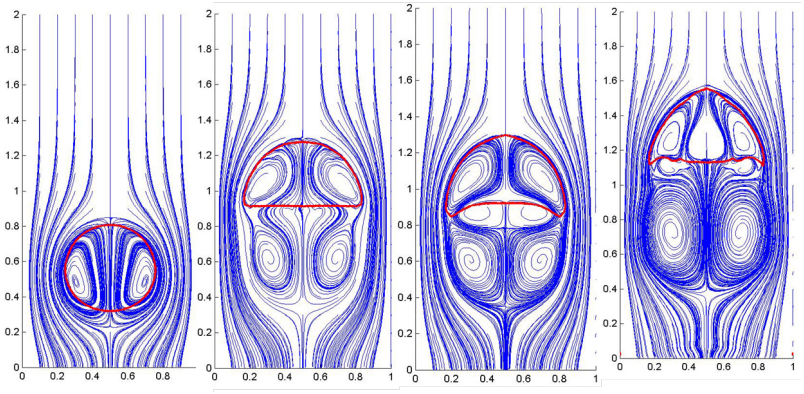

Figure 3.1: Different shape regimes (1 and 3)

Bubbles rising in a flow regime can be characterised by the non-dimensional numbers namely Eotvos (Eo), Morton (M), and Reynolds (Re):

$$Eo = g\Delta\rho\frac{d_{bubble}^2}{\sigma}, \tag{3.1}$$

$$M = g\mu_l^4\frac{\Delta\rho}{\rho_l^2}\sigma^3, \tag{3.2}$$

$$Re = \rho_l d_{bubble}\frac{u_T}{\mu_l}, \tag{3.3}$$

where, $\Delta\rho$ $[kg/m^3]$ is the difference in density of the two phases, g is the gravitational acceleration $[m/s^2]$, d_{bubble} [m] is the diameter of the bubble, σ is the surface tension $[N/m]$, μ_l [kg/ms] is the viscosity of the surrounding liquid, ρ_l $[kg/m^3]$ is the density of the surrounding liquid and u_T is the terminal velocity.

The terminal velocity is the steady velocity that a bubble can reach when the buoyancy and the drag forces are in equilibrium. For different bubble shapes a different formula for the terminal velocity is provided.

Here, the values of the Eotvos and Morton numbers are calculated. The values of the Eotvos number depending on the bubble diameter are shown in Table 3.1.

Bubble diameter (m)	Eotvos number
0.0005	0.13
0.001	0.53
0.002	2.14
0.003	4.83
0.004	8.59
0.005	13.42
0.006	19.33
0.007	26.31
0.008	34.37
0.003	43.50
0.01	53.7
0.015	120.8

Table 3.1: Eotvos number as a function of bubble diameter

The Morton number is calculated and logM equals to -9.6. According to those numbers and using the graph from Clift et al [23] the bubble shape depending on the bubble diameter is in the area of spherical, ellipsoidal and spherical cap bubbles (Fig. 3.2, [23]). The shape of the bubbles computed from the simulations shown in the following are in agreement with the expected shape from the graph.

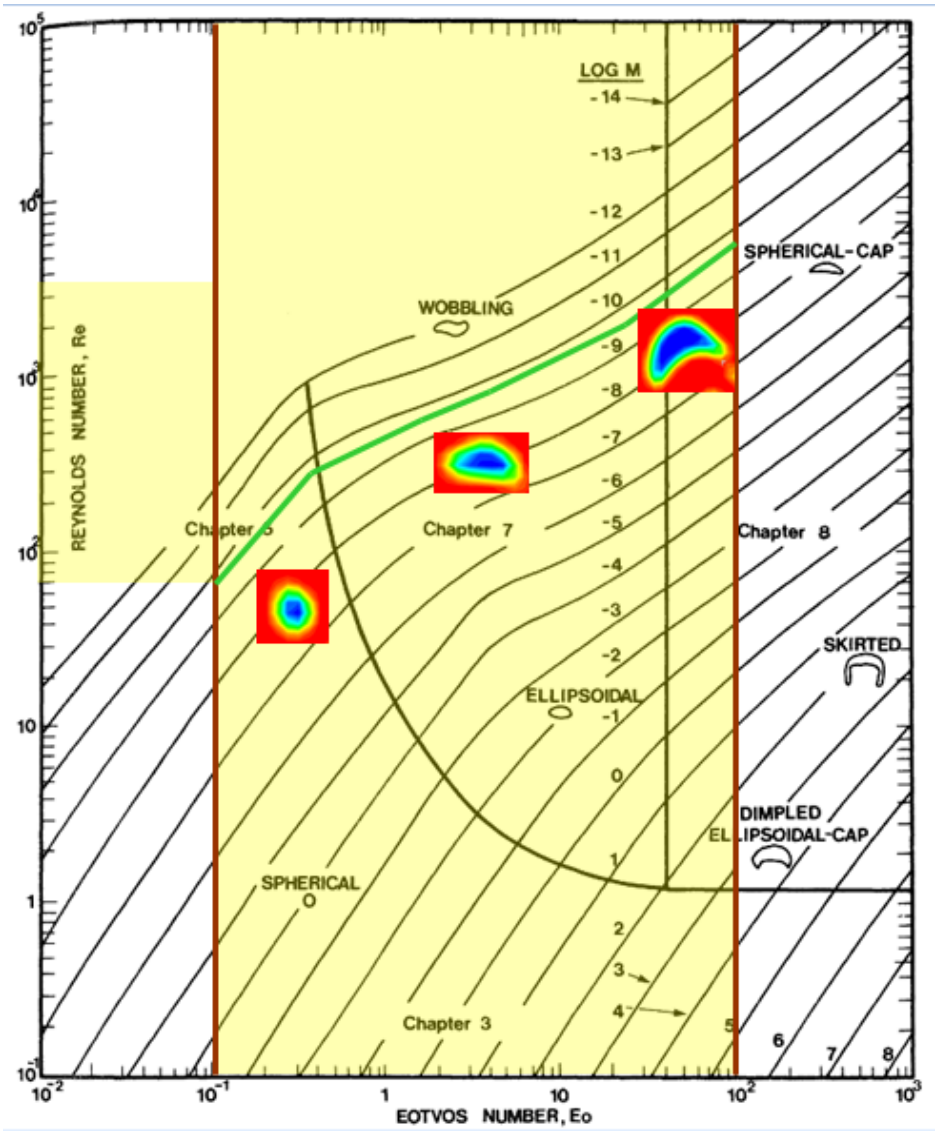

Figure 3.2: Bubble shapes

3.1.2 Description of the cases

Three different simulation categories of case studies have been performed. The first category (Category A) includes simulations with the original geometry with different boundary conditions (filling degree, cooling system). The second category (Category B) includes variations in the inlet flow rates and the third (Category C) different geometry modifications to optimize the current bubbler design. Most of the simulations run until a quasi-steady solution is obtained and the vapor mole fraction at the outlet, $< x_{tmg} >_{out}$, is monitored as well as the average vapor mole fraction in the gas, $< x_{tmg} >_{g}$, and the

average temperature, in the bubbler, $< T >$.

The volume average vapor mole fractions and temperatures are calculated by:

$$< x_{tmg} >_{out} = \frac{1}{A_{out}} \int_{A_{out}} x_{tmg} dA, \tag{3.4}$$

$$< x_{tmg} >_{g} = \frac{\frac{1}{V_b} \int_{V_b} \alpha_g x_{tmg} dV}{\frac{1}{V_b} \int_{V_b} \alpha_g dV}, \tag{3.5}$$

and

$$< T >= \frac{1}{V_b} \int_{V_b} T dV, \tag{3.6}$$

where, A_{out} $[m^2]$ is the area of the outlet and V_b $[m^3]$ is the bubbler volume.

3.1.3 Category A

The cases that are used in this section are listed in Table 3.2

Cases	Description
A_1	original geometry - no condensation at the walls
A_2	original geometry - condensation at the walls
A_3	modified geometry - condensation at the walls
A_4	original geometry- cooling system at the walls
A_5	original geometry - higher temperature on the top

Table 3.2: Properties used for the Case studies A

Case Studies: Low filling degree: A_1, A_2, A_3

Condensation at the walls

During the filling process experimental measurements were used to validate the model. Even at low filling degree ($< 20\%$) the measured vapor concentration was close to the equilibrium value even for flow rates up to 2000 sccm. Therefore simulations of the original geometry using a low filling degree (operating conditions are shown in Table 3.3), with

two boundary conditions (condensation at walls, no condensation at walls) are performed and compared.

Properties	Value
Filling degree	20%
Inlet flow rates (sccm)	2000
Inlet temperature (^oC)	T_{in_A}
S	0.9
Operating temperature (^oC)	T_{op_A}
Operating pressure (Pa)	p_{op}

Table 3.3: Properties used for the Category A

Comparison between the two different cases A_1 and A_2 is presented in Figures 3.3 and 3.4. It is shown that condensation at the walls during the filling process is a very important mechanism to reach equilibrium. Almost all the incoming supersaturated gas is condensed in the feed pipe before it enters into the bubbler.

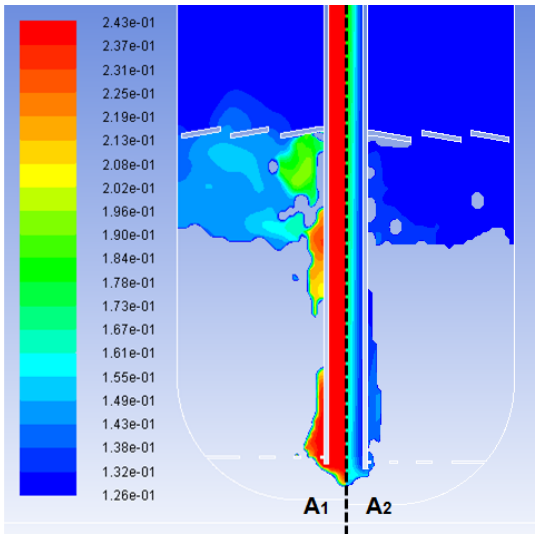

Figure 3.3: Gas phase vapor mole fraction comparison between the Cases A_1 and A_2 at t=1sec

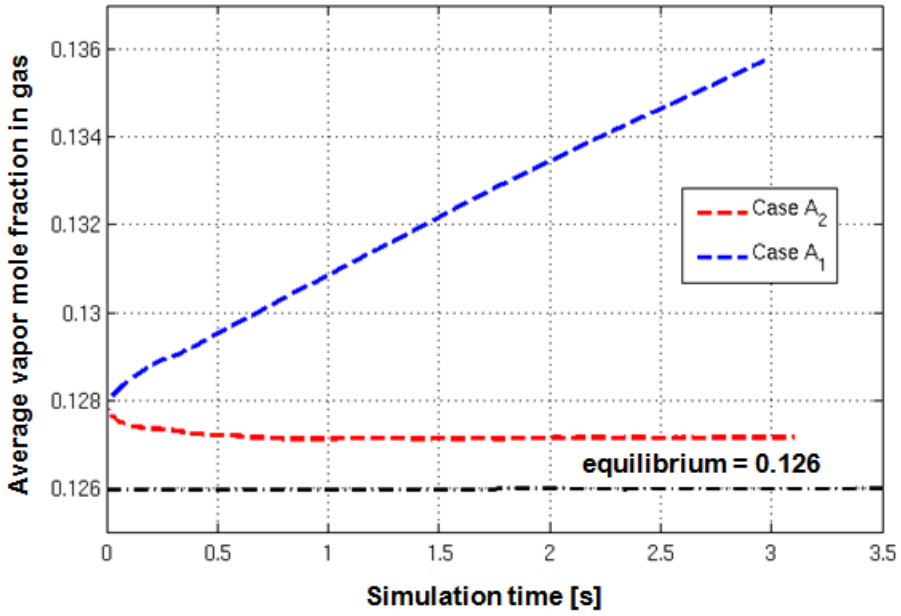

Figure 3.4: Comparison between imposing equilibrium value at the walls

Comparison between original (Case A_2) and modified geometry (Case A_3)

A modified geometry (Case A_3) was first tried in that filling degree ($< 20\%$). An additional internal was added halfway between the perforated plate and the first internals. The idea was to give the bubbles higher residence time in the liquid. However, no improvement was evident. The gas rising at the feed pipe in the unmodified geometry at such low filling degree creates a jet of liquid which collides with the first row of internals. The jet then breaks up in small droplets (Cases A_1 and A_2 in Fig. 3.5). By forming droplets apparently sufficient interfacial area for mass transfer is created. This masks the benefit of residence time increase for bubbles in the liquid due to the geometry modification (Case A_3 in Fig. 3.5). Note however, that the droplet formation phenomenon is not present at higher filling degrees at which the bubbler is normally operated (e.g. Fig. 3.24).

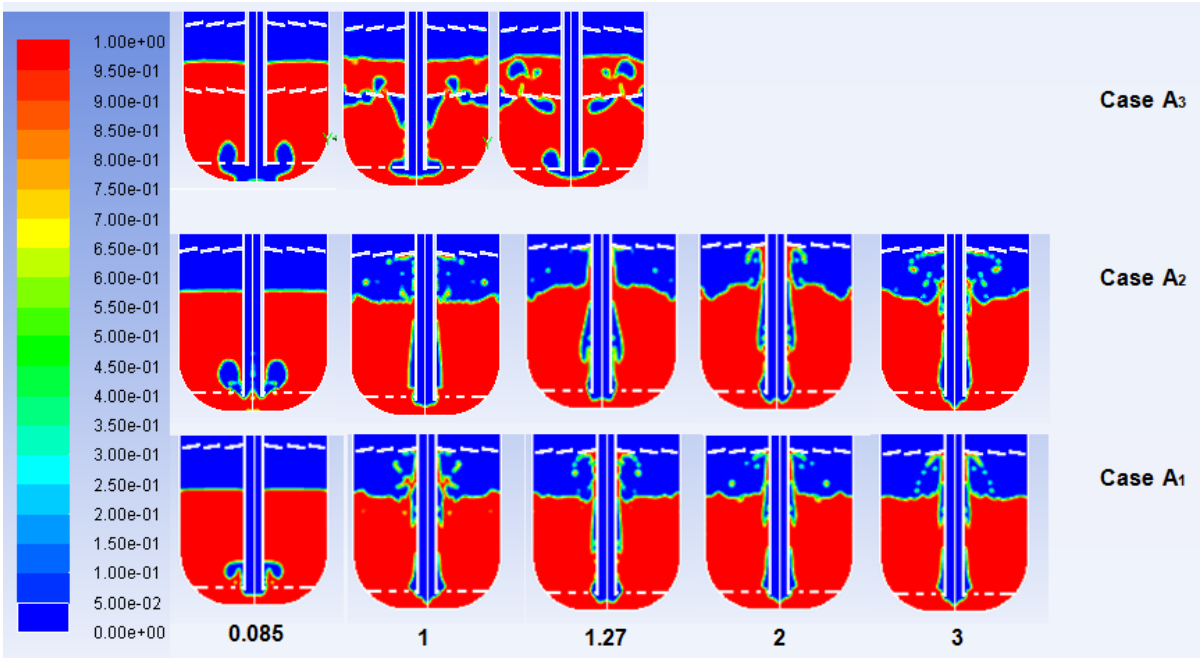

Figure 3.5: Liquid volume fraction comparison between Cases A_1, A_2, A_3

Case Studies: High filling degree, reference case, A_4 ***and*** A_5

Reference case: C

Reference case refers to the original geometry with the operating conditions shown in Table 3.4. This case is used for comparison.

Properties	Value
Filling degree	80%
Inlet flow rates (sccm)	3500
Inlet temperature (^oC)	T_{in}
S	0.9
Operating temperature (^oC)	T_{op}
Operating pressure (Pa)	p_{op}

Table 3.4: Boundary conditions used for the reference case

Case A_4: Cooling of the walls

In this section a cooling system is applied at the walls of the original geometry and a heat transfer coefficient of $h_{ex} = 15000W/m^2K$ and an external temperature of $T_{ex} < T_{op}$ were imposed. Other boundary conditions are as defined for the reference case.

The results show that by imposing a cooling system at the outer walls, the liquid temperature decreases from its initial value; negative values in Fig. 3.6 indicate that temperature is lower than T_{op}, while using adiabatic walls the temperature increases slightly due to condensation. The following results show the worst case scenario for temperature increase (Fig. 3.7).

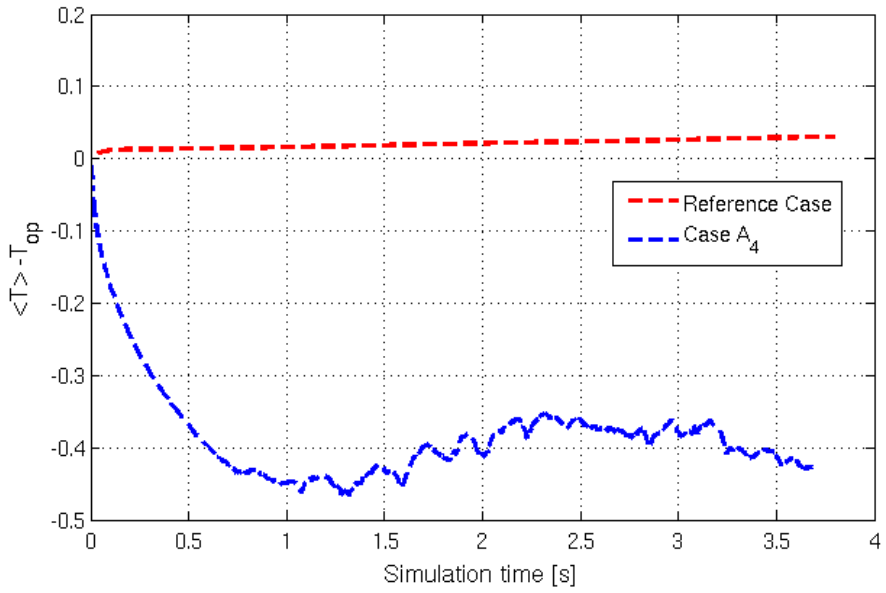

Figure 3.6: Comparison of the temperature distribution

Figure 3.7 shows how the temperature affects the average mole fraction of the vapor. As shown above the cooling system reduces the average bubbler temperature slightly. As expected the mole fraction in Case A_4 is lower then in the reference case because the equilibrium vapor mole fraction decreases by decreasing the temperature.

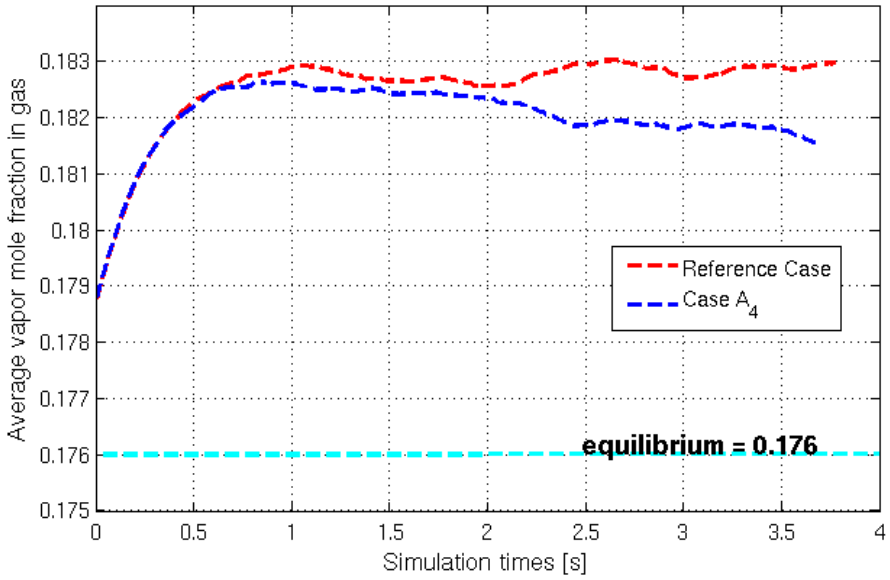

Figure 3.7: Average vapor mole fraction in gas versus simulation time

Case A_5: High temperature on the top

In this case a higher temperature is imposed on the top of the bubbler because the actual cooling system does only cool parts of the bubbler but not the top which is exposed to ambient temperature (Fig. 3.8). This case is compared with the reference case. In the experiments condensed water is observed on the top of the bubbler.

Figure 3.9 shows the increment of the temperature inside the bubbler and Fig. 3.10 the comparison of the corresponding vapor mole fractions.

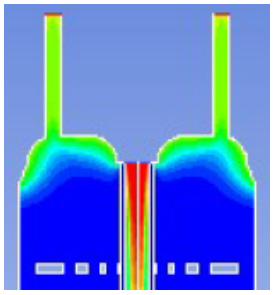

Figure 3.8: Higher temperature on top, contours of temperature, Case A_5

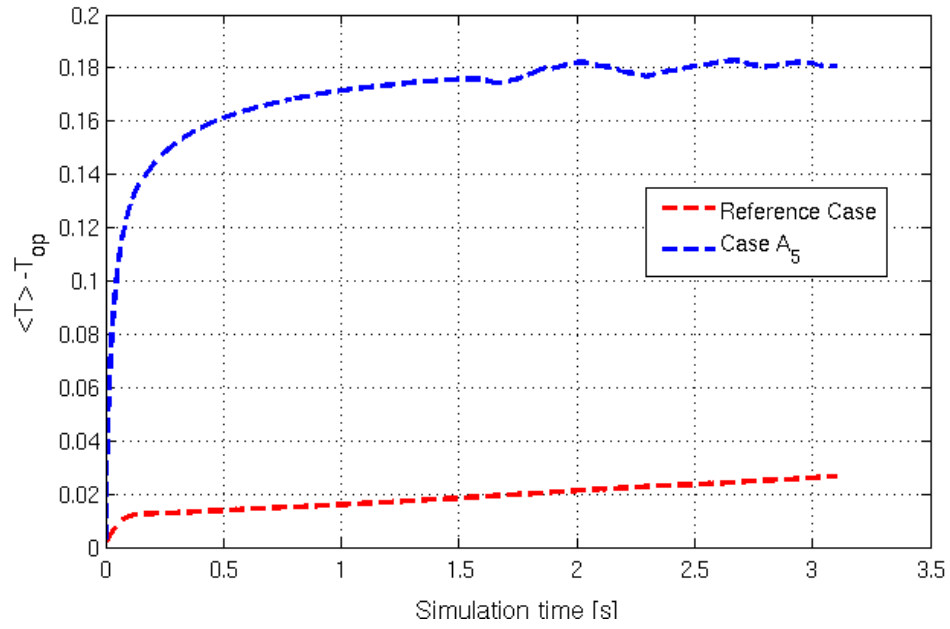

Figure 3.9: Comparison between reference case and Case A_5

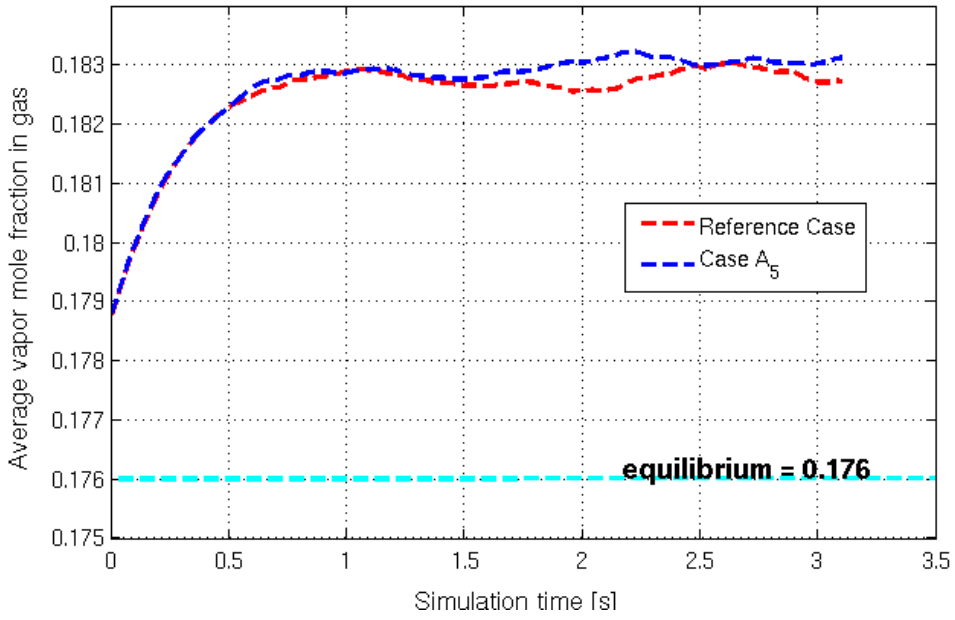

Figure 3.10: Comparison between reference case and Case A_5

In the figures above, the influx through the bubbler-top in Case A_5 does not affect significantly the average bubbler temperature ($< 0.2^0C$). Also, the vapor mole fraction increases only slightly, as expected (< 0.001).

Finally, as shown in Category A, temperature differences in the reactor due to condensation and cooling are small compared to the operating temperature and in the following the simulations use adiabatic walls as boundary conditions. This is the worst case scenario for temperature increase.

Assuming that the inlet saturation degree is 0.9, the heat generated in the bubbler if all vapor that exceeds the vapor equilibrium saturation would condensate, ($Q_{condensation}$ [W]) is calculated by the formula below:

$$Q_{condensation} = \Delta H_{vap} Q_{0tmg} = 3.4W, \tag{3.7}$$

The heat loss from bubbler to the cooling system is calculated using the known water flow rate ($\dot{m}$, [kg/s]), the measured temperature difference (ΔT) between inlet and outlet temperatures of the cooling circut, and the specific heat of the water (C_p, [J/kgK]).

$$Q_{cooling} = \dot{m} C_p \Delta T = 51W. \tag{3.8}$$

From the above calculations it is evident that heat which has to be extracted from the bubbler due to condensation is 3.4W. The current cooling system extracts 51W. Thus the cooling system is sufficient enough to keep the bubbler at a constant temperature.

3.1.4 Case Studies B

In the current category the original geometry is used and different inlet flow rates were tried.

Case	Inlet Flow Rates [sccm]
B_1	50
B_2	1000
B_3	2000
B_4	3500

Table 3.5: Properties used for the Category B cases

The operating conditions are summarized in the following Table 3.6

Properties	Value
Filling degree	80%
Inlet flow rates (sccm)	$50, 1000, 2000, 3500$
Inlet temperature (^oC)	T_{in_B}
S	0.9
Operating temperature (^oC)	T_{op}
Operating pressure (Pa)	p_{op}

Table 3.6: Properties used for the Category B

Figure 3.11 shows the vapor mole fraction for different flow rates. Because the mole fraction is volume-averaged and the equilibrium value patched in the gas phase at t=0 (except in the inlet pipe), the initial average mole fraction is a little higher than the equilibrium value and the mole fraction starts increasing as the supersaturated gas enters.

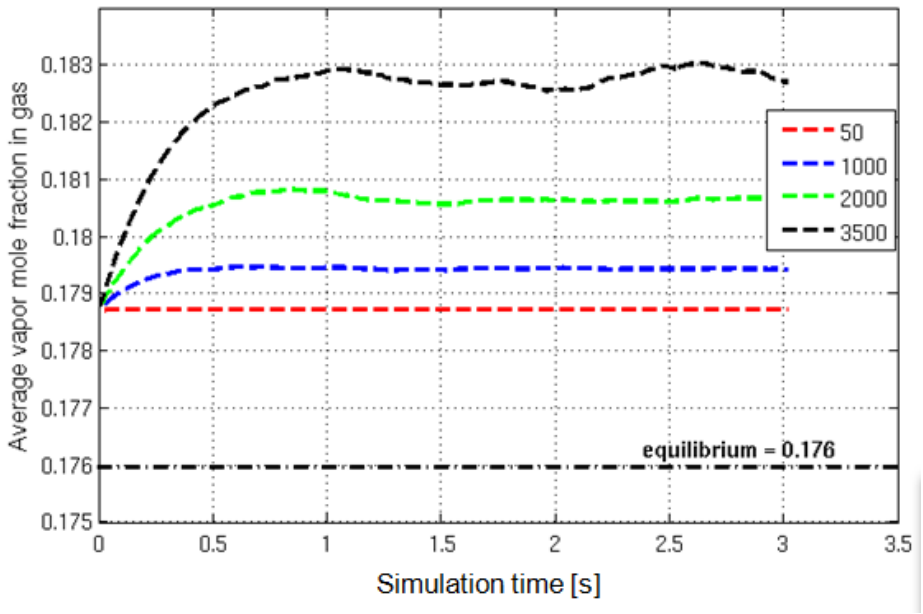

Figure 3.11: Comparison of the vapor mole fraction for different flow rates versus simulation time

It is observed that the mole fraction increases at the begining and then seems to fluctuate around a constant value thus having reached statistically steady-state conditions. This happens approximately after 3 s. As higher the flow rate as higher is the final mole fraction value, because more supersaturated gas enters into the bubbler with increasing flow rate. In general, however, differences in the mole fraction are small and close to the equilibrium value (Fig.3.12, < 0.007).

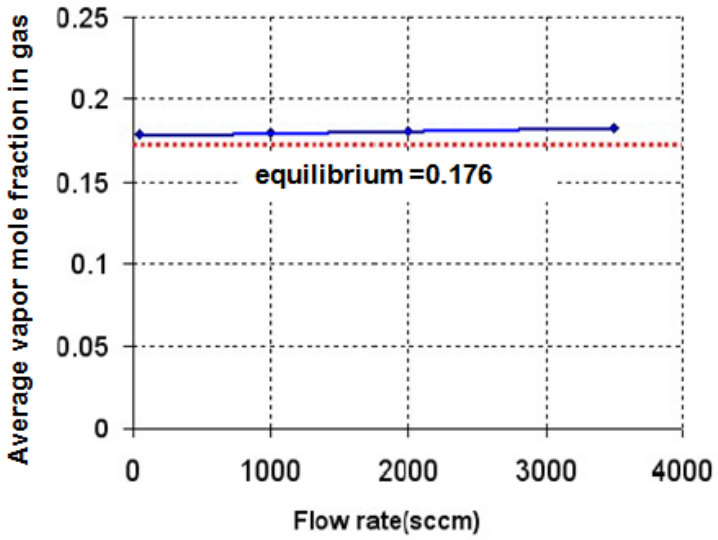

Figure 3.12: Average vapor mole fraction for different flow rates at t=3 s

In Fig. 3.13 to Fig. 3.16 the contours of vapor mole fraction at different times and flow rates are given. The supersaturated gas (red) enters into the bubbler and condensates while rising in the bubbler and comes close to the equilibrium value for the bubbler temperature (blue colour). Note that the transparent regions are filled with liquid, so the figures also show the phase distribution.

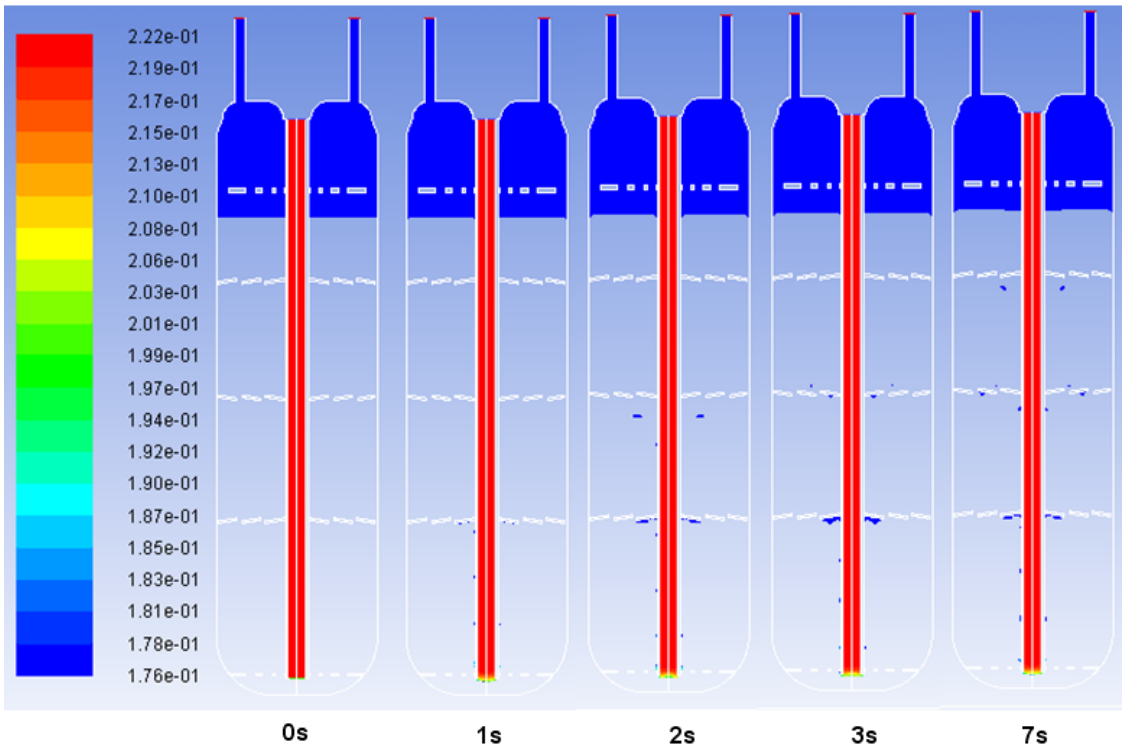

Figure 3.13: Contours of vapor mole fraction with 50 sccm inlet flow rate

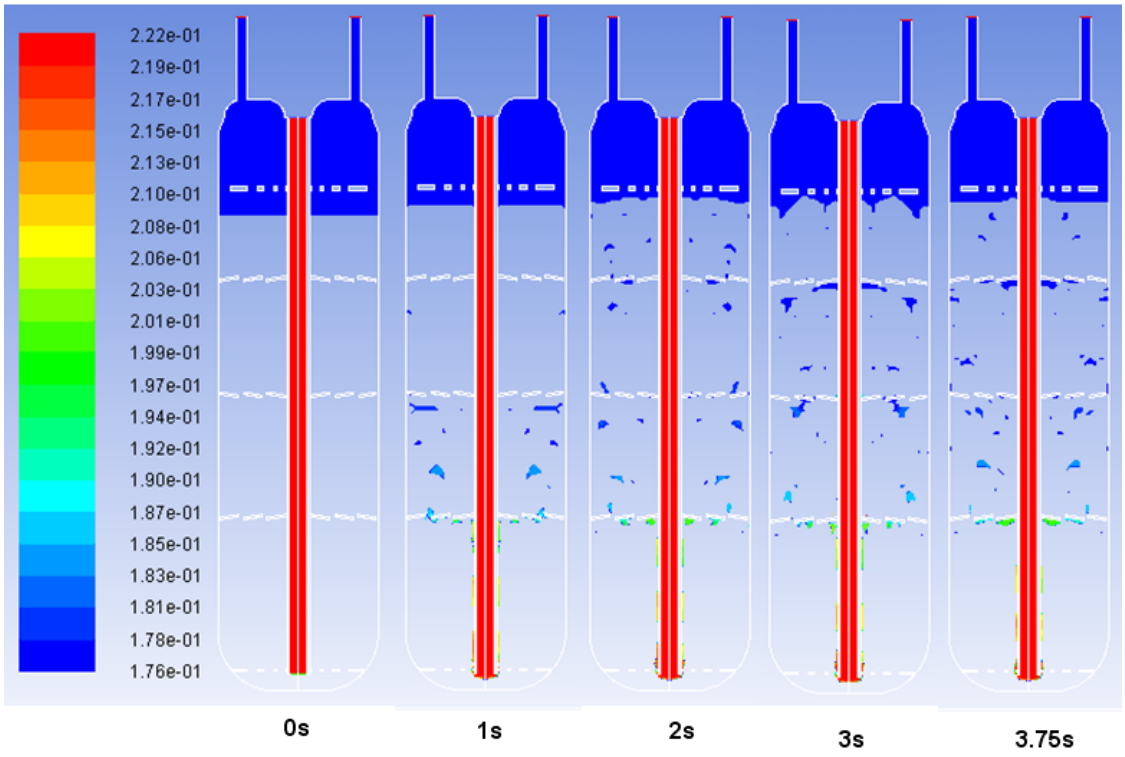

Figure 3.14: Contours of vapor mole fraction with 1000 sccm inlet flow rate

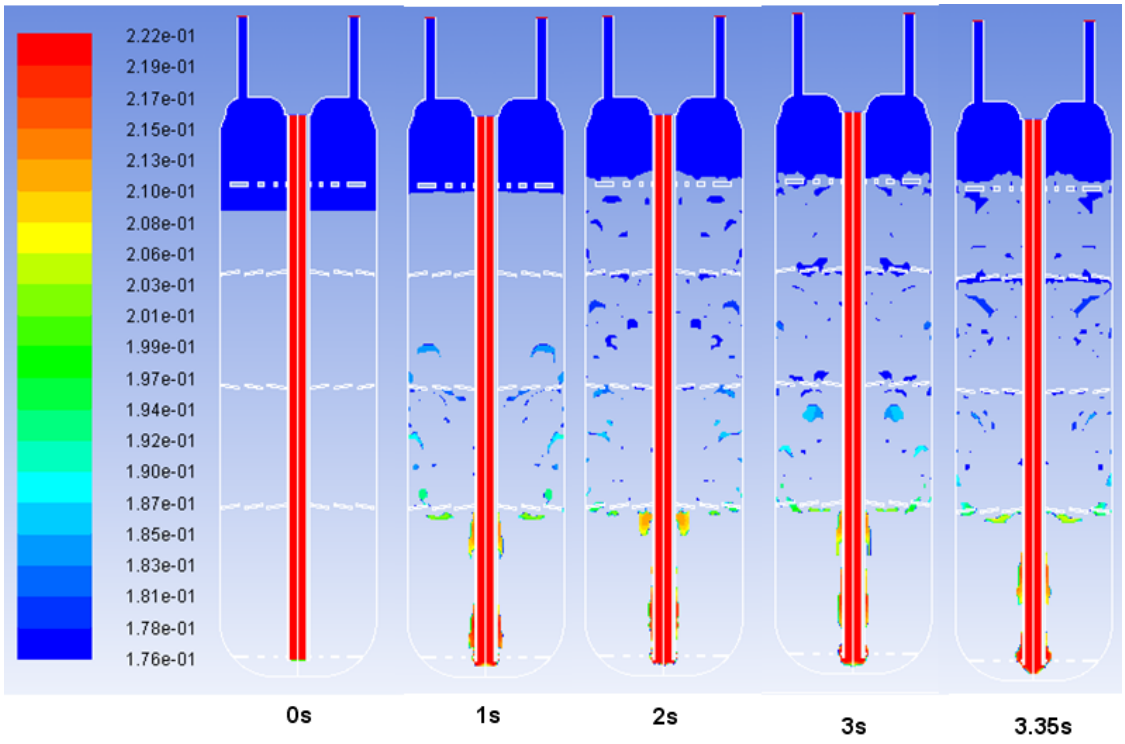

Figure 3.15: Contours of vapor mole fraction with 2000 sccm inlet flow rate

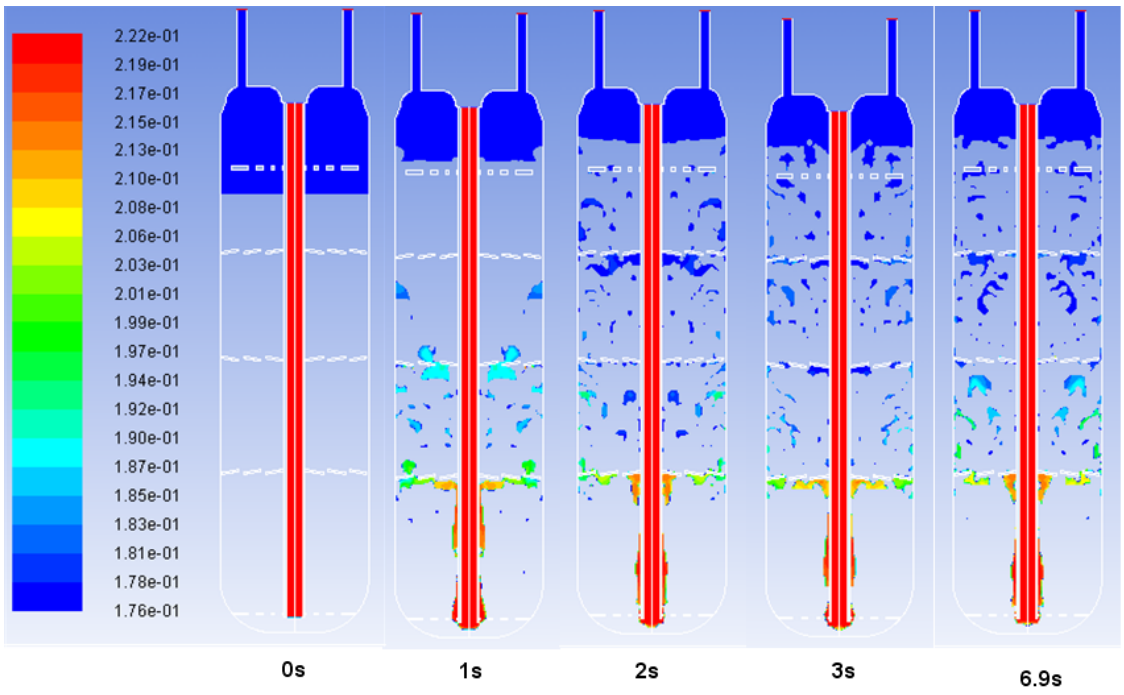

Figure 3.16: Contours of vapor mole fraction with 3500 sccm inlet flow rate

The difference in the height of the liquid free surface between initial and statistically steady-state conditions represents the volume fraction of the gas inside the liquid. This parameter is called gas hold-up and is calculated as:

$$\alpha_g = \frac{\Delta V}{V_0 + \Delta V} \tag{3.9}$$

where, V_0 $[m^3]$ is the initial volume of liquid, ΔV is the liquid volume due to the free surface movement and is calculated as:

$$\Delta V = \pi H (R^2_{bubbler} - R^2_{pipe}) \tag{3.10}$$

where H [m] is the height difference as explained above, $R_{bubbler}$ [m] is the bubbler radius, R_{pipe} [m], is the inlet's pipe radius.

Figure 3.17 shows that at high inlet flow rates more gas is "held" inside the liquid and moves, thus increases the level of the free surface more compared to lower inlet flow rates.

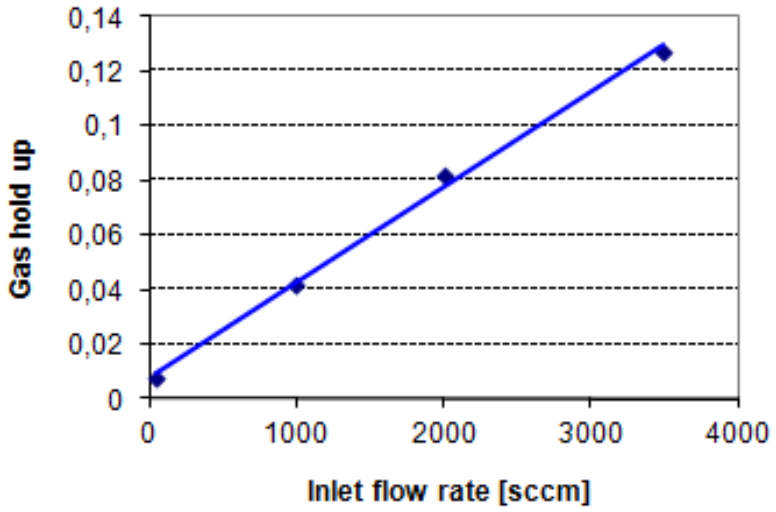

Figure 3.17: Gas hold up for different inlet flow rates

In the figures above it is shown that at low flow rates, few small bubbles appear and that the time that the first bubble needs to reach the free surface is higher compared to the other cases. As the inlet flow rate increases more gas enters into the bubbler and "pushes" the first bubbles to reach the surface faster Table (3.7).

Inlet Flow Rate [sccm]	time[s]
50	2.5
1000	2
2000	1.5
3500	1.3

Table 3.7: Time for the first bubble to reach the free surface

Therefore, the case with 3500 sccm inlet flow rate reaches statistically steady-state conditions, characterized by a constant liquid level, faster.

Temperature increases by increasing the inlet flow rate because more gas with temperature higher than the bubbler temperature enters the bubbler (Fig. 3.18).

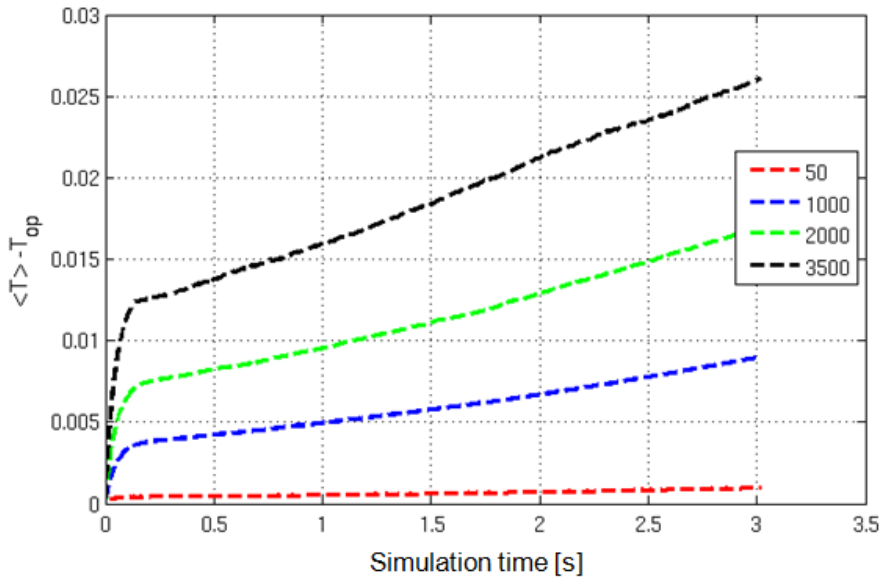

Figure 3.18: Comparison of the temperature distribution for different flow rates

The pressure drop in the bubbler system from inlet to outlet for the different inlet flow rates is given in Table 3.8; it becomes clear that the highest flow rate has the highest pressure drop.

Inlet Flow Rates [sccm]	Pressure drop [Pa]
50	2273.9
1000	2295.9
2000	2309.6
3500	2312.4

Table 3.8: Pressure drop in the bubbler for different inlet flow rates

Finally, as it is shown in the Categories A and B, the section between the lower perforated plate and the first internal does not increase the residence time and does not create much interface, thus is not active in promoting condensation. Here, an improvement seems possible by adding an additional internal and by closing the first hole in the perforated plate (Fig. 3.19).

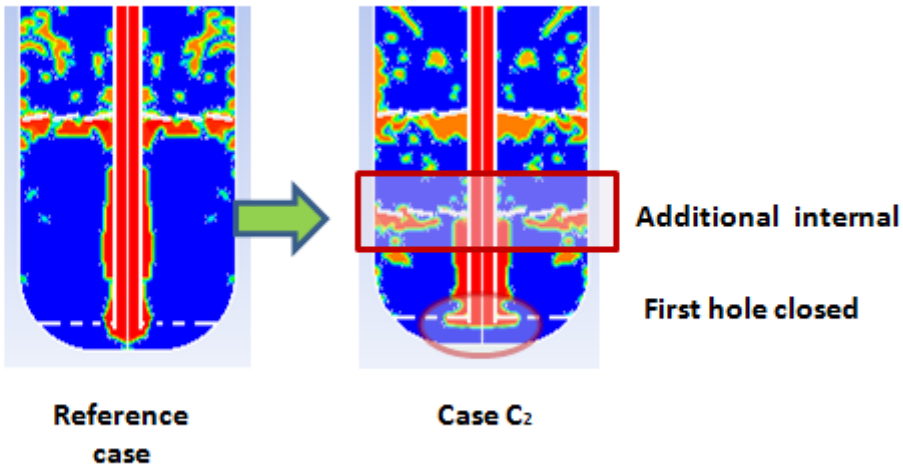

Figure 3.19: Possible geometrical improvement

3.1.5 Case Studies C

In these case studies the operating conditions used for the simulations remain constant as in the Numerical Part, e.g. the inlet flow rate is 3500 sccm. Instead of process parameter variations, modifications of the internal design (Fig. 3.20), and bubbler diameter and heights (Fig. 3.21) are tried. Simulation results should give information that allow optimization of the current bubbler design, Table 3.9.

Case	Geometry description
C_1	Internal addition and one perforated hole closed
C_2	Internals replaced by perforated plates
C_3	The height of the bubbler increased
C_4	The height of the bubbler decreased
C_5	The diameter of the bubbler increased

Table 3.9: Description of the modified geometries

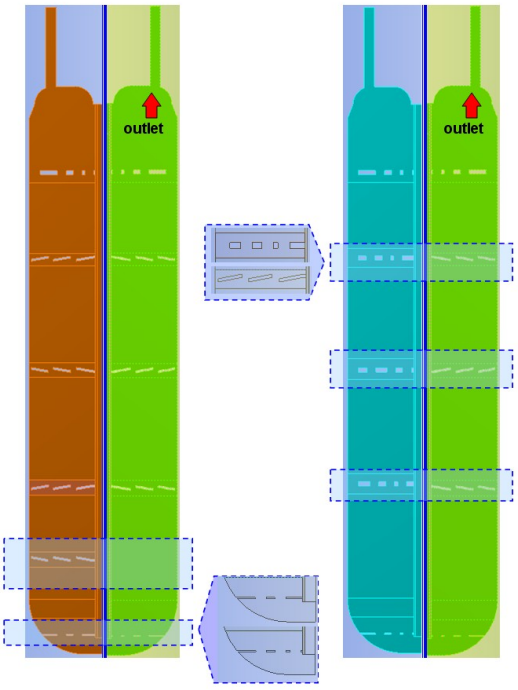

Figure 3.20: Different geometries Case C_1 and Case C_2 in comparison with the reference case (C, green)

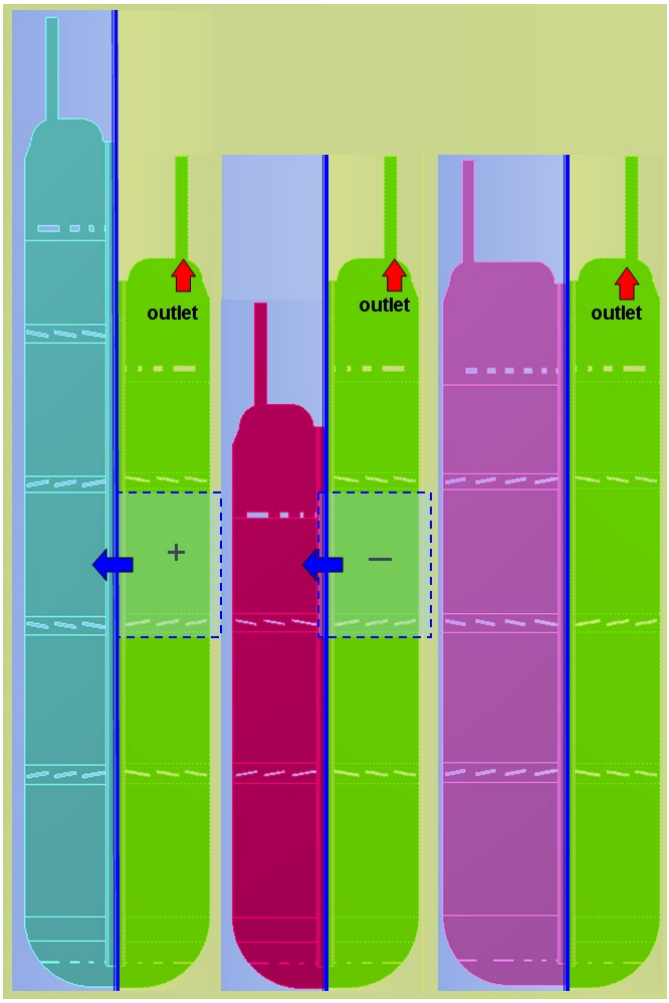

Figure 3.21: Different geometries Cases C_3, C_4 and C_5 in comparison with the reference case (C, green)

The operating conditions summarized in Table 3.10

Properties	Value
Filling degree	80%
Inlet flow rate (sccm)	3500
Inlet temperature (^oC)	T_{in}
S	0.9
Operating temperature (^oC)	T_{op}
Operating pressure (Pa)	p_{op}

Table 3.10: Properties used for the Category C

The comparison of the simulation results for the above geometries are summarized in the figure below.

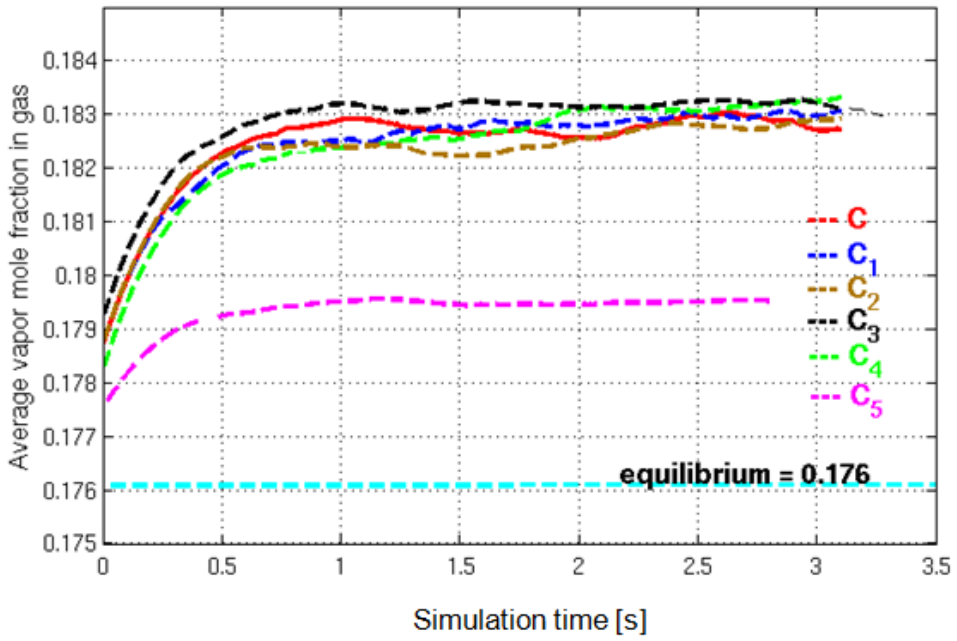

Figure 3.22: Comparison of average vapor mole fraction for different geometries

As shown in Fig. 3.22 the variations of the average vapor mole fraction between the different geometries are small. According to the figure, the geometry with the larger bubbler diameter (C_5) gives values closer to the equilibrium. However, the difference between the bubbler with the larger diameter with the other configurations is not very high (< 0.004). The larger the bubbler diameter the higher the residence time between the two internals (e.g. Fig. 3.28) for a bubble which follows the circulating flow .

It is concluded that the reference bubbler design already is very good.

Figure 3.23 compares the reference case with the Case C_1. The bubbles in Case C_1 are reach the equilibrium vapor mole fraction much faster (blue colour). Due to the additional internal, bubble residence time increases and the bubbles reach the equilibrium value already at the first series of internals.

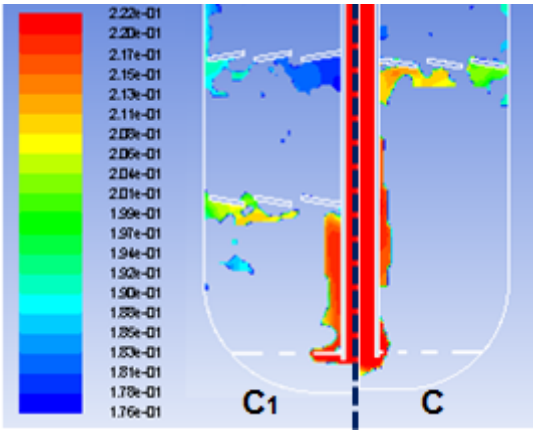

Figure 3.23: Contours of vapor mole fraction for Case C_1 (left) and reference case (C, right)

In Fig. 3.24 to Fig. 3.28 the vapor mole fraction is presented for the different geometry configurations.

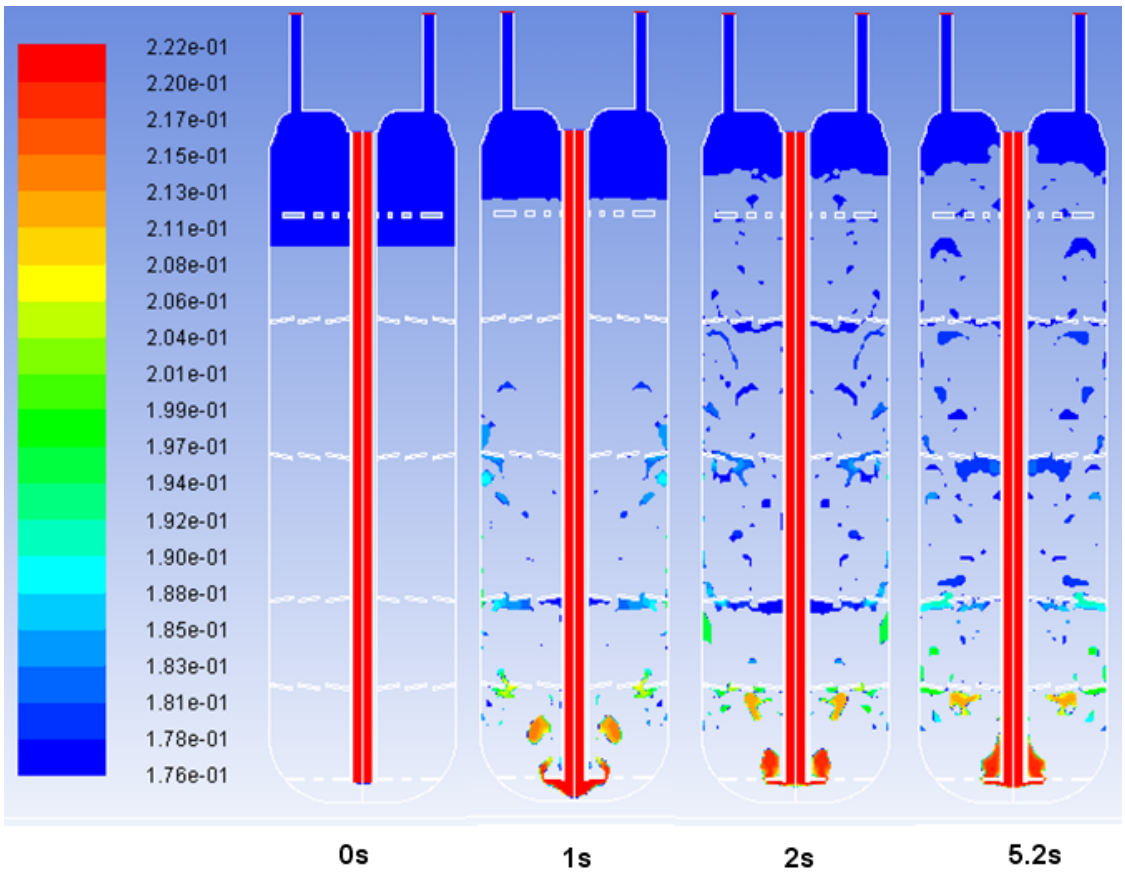

Figure 3.24: Contours of vapor mole fraction for case C_1 (additional internal)

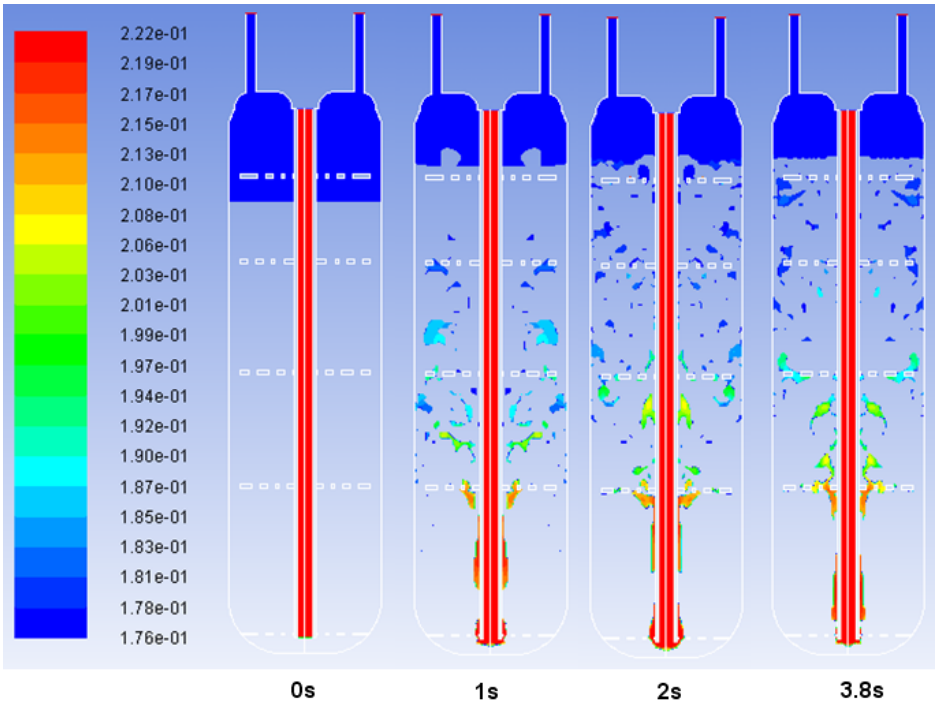

Figure 3.25: Contours of vapor mole fraction for case C_2 (perforated plates)

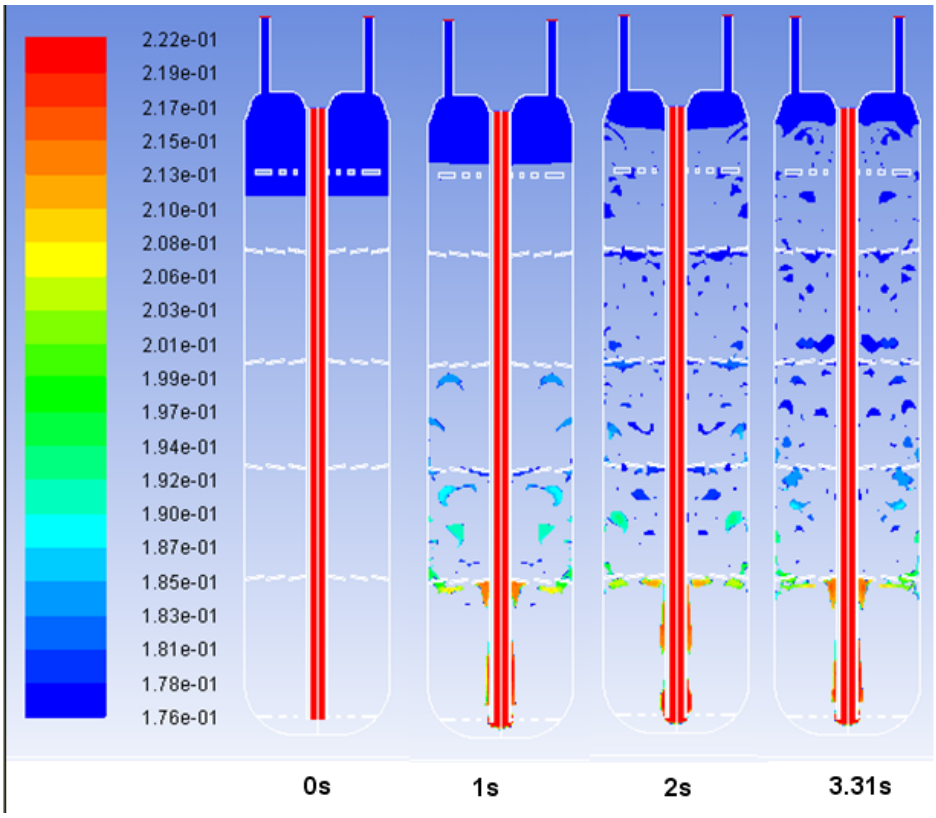

Figure 3.26: Contours of vapor mole fraction for case C_3 (increased bubbler height)

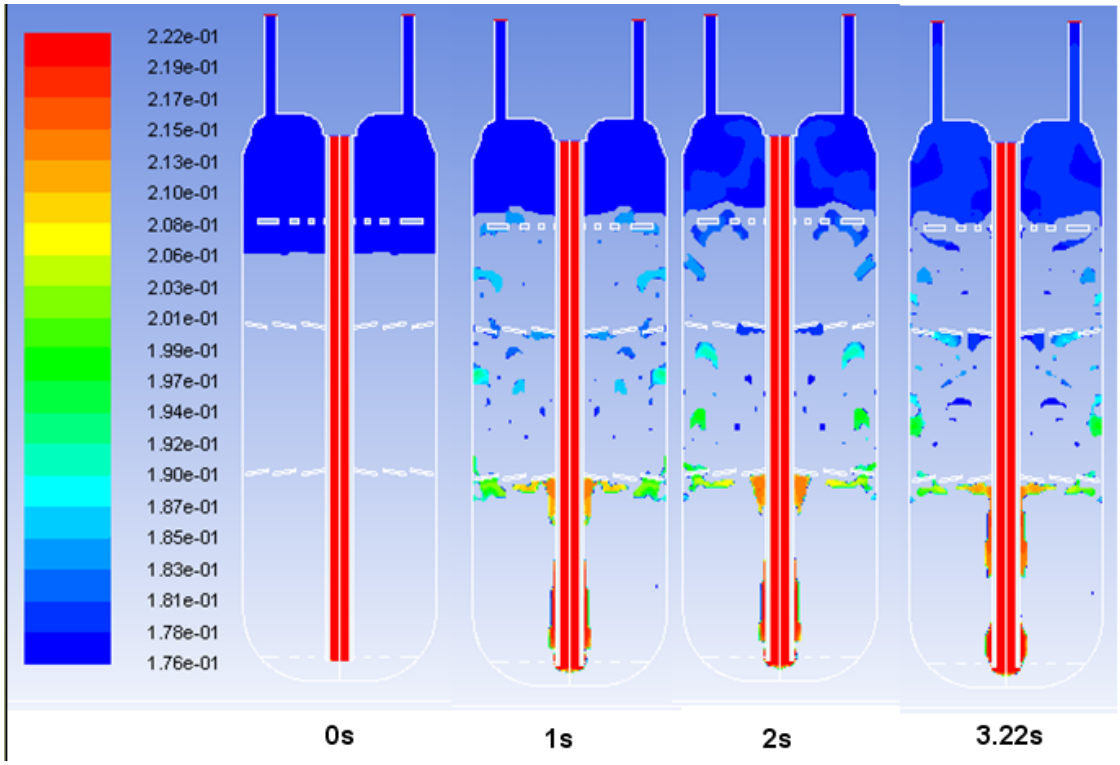

Figure 3.27: Contours of vapor mole fraction for case C_4 (reduced bubbler height)

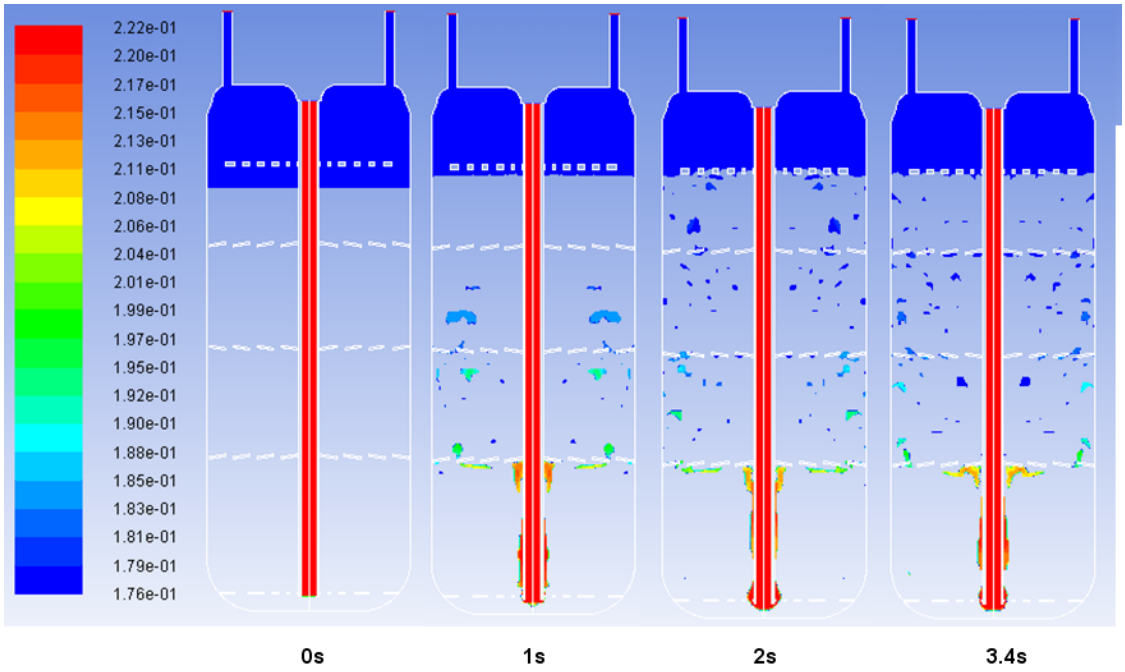

Figure 3.28: Contours of vapor mole fraction for case C_5 (increased diameter)

The contours of vapor mole fraction in Fig. 3.29 shows that Case C_1 saturates the

gas phase faster than the other geometries. Case C_4 yields the worst result because the residence time decreases.

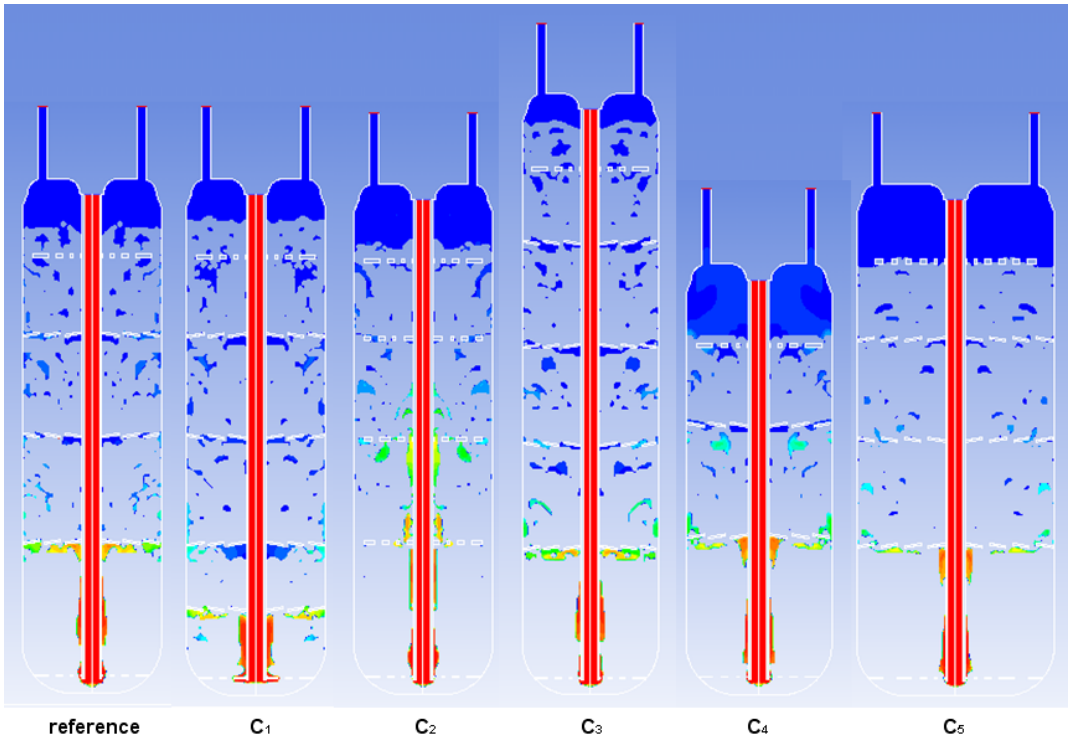

Figure 3.29: Contours of vapor mole fraction for the different cases at $t = 3s$

The average mole fraction at the outlet, i.e. the value going to the MOCVD reactor, is given in Fig 3.30. As it is observed, geometry C_4 (reduced bubbler height) has the highest mole fraction which is expected due to the geometric characteristics. Among the other designs, C_5 and C_3 are closed to the equilibrium values because they have probably the highest residence time due to their increased liquid volume compared to the other cases. However, because metallorganic liquid stored in the bubbler is expensive, and because the final mole fraction value of Case C_1 (additional internal) is also very close to the Case C_3 and Case C_5, Case C_1 is considered the best.

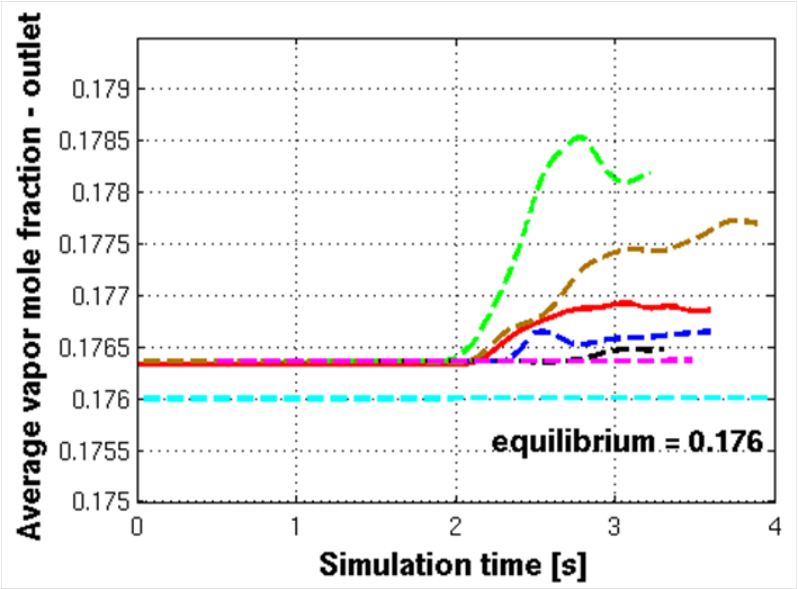

Figure 3.30: Average vapor mole fraction at the outlet versus simulation time

The temperature distribution in the different geometries is shown in the Fig. 3.31. The temperature remains almost constant in the whole domain although evaporation and condensation extract and heat up locally the surrounding liquid. The inlet temperature has only a small effect on the rest of the bubbler (Fig. 3.32). Here, some condensation sets in at the bottom of the pipe and condensation elsewhere is observed mainly between the lower perforated plate and the second internal above it. As shown, increasing inlet temperature heats up locally the top of the bubbler.

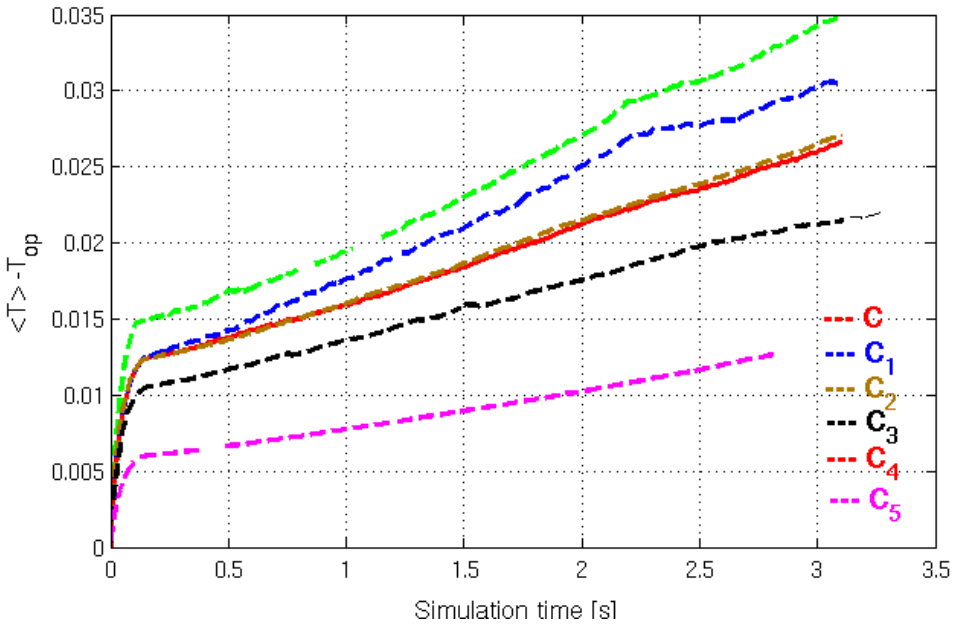

Figure 3.31: Comparison of average T for different geometries

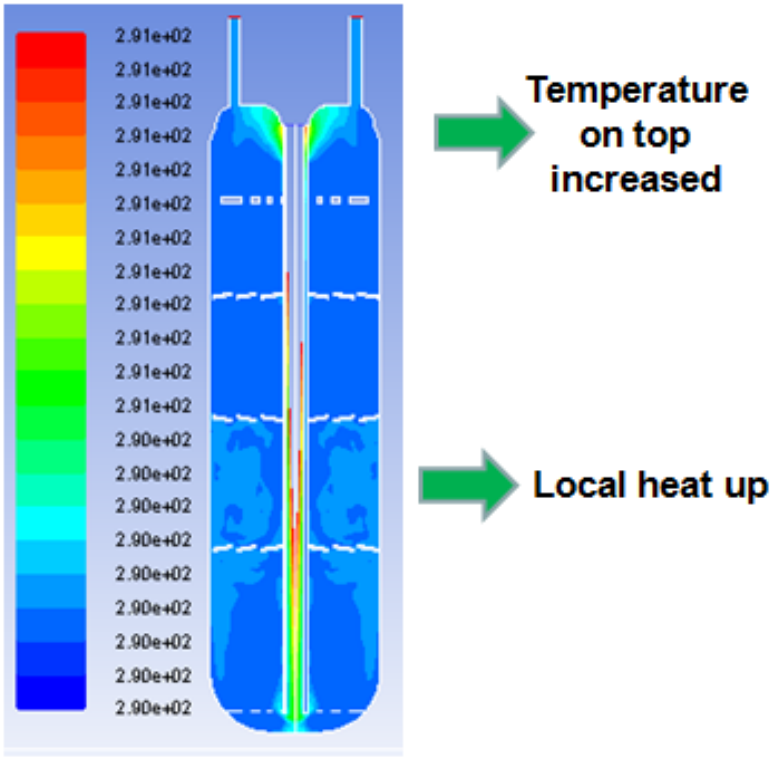

Figure 3.32: Contours of temperature for the reference case

Again all temperature increases are small ($< 0.1^0C$).

The pressure drop for the different geometries types is listed in Table 3.11

Geometry type	Pressure drop [Pa]
C	2343.9
C_1	2409.05
C_2	2609.06
C_3	3004.4
C_4	1674.6
C_5	2312.3

Table 3.11: Pressure drop in the bubbler for different geometries

Again the values are small compared to the operating pressure, so it seems justified to neglect the effect of dynamic pressure on the equilibrium vapor mole fraction.

The gas hold up in these cases is shown in Fig. 3.33. High value of gas volume fraction in the liquid TMG can be associated with high residence time of the gas inside the bubbler. In the Fig. 3.33 the gas hold up has the highest value in Case C_1 (additional internals) and the lowest in Case C_5 (increased bubbler diameter). That happens because the free surface moves very slowly in Case C_5, and the computational time needed might be very high to be represented in this study.

Of the three cases with the same bubbler volume, Cases C_1, C_2 and reference C, clearly C_1 is the best due to the additional internal (Fig. 3.33)

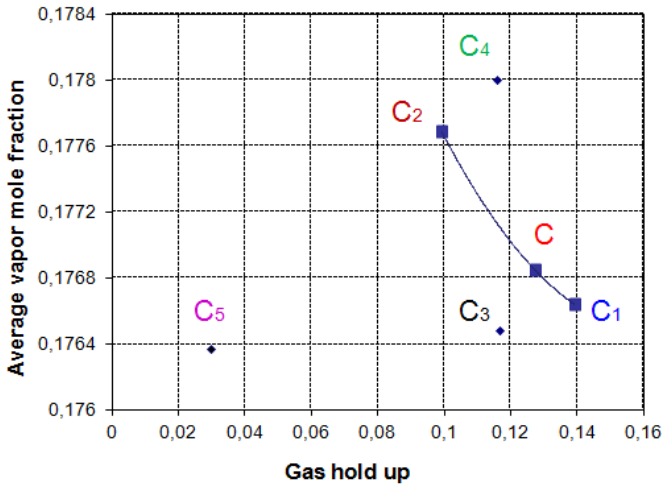

Figure 3.33: Comparison between the gas hold up of different modifications

Figure 3.34 shows the streamlines for the different geometries. In Case C_1 (additional internals) there are more recirculation cells, thus bubbles have higher residence time compared to the other cases. Clearly, addition of an internal to the other cases would also increase residence time there.

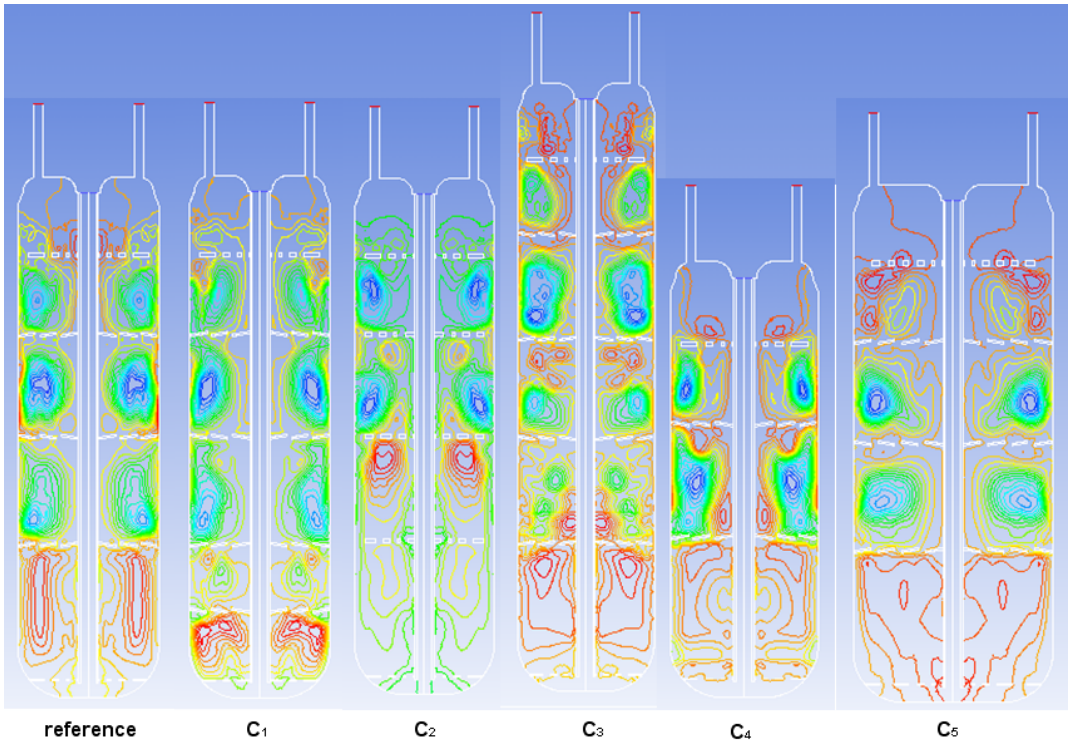

Figure 3.34: Streamlines for the different geometries at $t = 3s$

3.2 Conclusions

An optimization study on a new prototype bubbler system, used in metalorganic chemical vapor deposition processes, is carried out by means of Computational Fluid Dynamics (CFD) analysis. The mass transfer model employed accounts for the evaporation and condensation of vapor which enters into a metalorganic source liquid.

The new bubbler system consists of two bubblers in series. The first one, which is a typical commercial bubbler, is used to saturate the carrier gas with vapor. The second is operated at a lower temperature so that the enterirng vapor condensates. It was the second bubbler that was simulated by CFD analysis and the model used was validated with a corresponding one for Stefan's problem. Three different categories of cases were simulated:

1. Category A:

   (a) Cases with low liquid filling degree in the bubbler in conjuction with condensation at the walls. The results show that, during the filling process, condensation at the feed pipe affects significantly equilibrium reaching at the bubbler outlet. The numerical results with regard to equilibrium vapor mole fraction at the outlet coincide with the experimental ones.

   (b) Cases with high liquid filling degree in conjuction with a cooling system and higher temperature at the top. These simulations did show that the installed cooling system is sufficient, because the extracted heat is higher than the heat generated by condensation whereas temperature increments remained below 0.1^0C.

2. Category B: Cases with different inlet flow rates of carrier gas and vapor precursor. It comes out that even for high flow rates a constant source flow is generated at the outlet, in accordance with the experimental results. Also, it became clear that the lower section in the bubbler is not practically effective because it does not increase the residence time and does not create much interface. Therefore, improvement was carried out by adding additional internals and by closing the first hole in the perforated plate. The pressure drop and the gas hold up increase as a function of inlet flow rate.

3. Category C: Cases with different geometry modifications. Special modifications to the characteristics of the geometry have been made. Higher, smaller, wider and modified types concerning the internals and perforated plates have been used so as to determine the most efficient geometry choice. For the implemented geometries shown in Chapter 3 it is concluded that all of the results obtained are similar. This suggests that the existing bubbler (reference geometry) is already close to be optimal. With regard to the reference bubbler, reducing bubbler height has to be avoided because it decreases the residence time. Wider bubblers lead to improved operation since they increase the residence time. As for the cost, the requiring storage for increased quantities of an expensive liquid is a disadvantage.

In summary, an actual improvement based on a modified geometry in which the addition of series of internals and the closure of the hole at the perforated plate, guides the system faster to the equilibrium value. This comes out to be the optimal bubbler design within the range of the examined cases.

With regard to computational requirements, the simulations reported in this thesis, which involve multiphase transient flow phenomena with mass transfer, are time consuming. The high computing power required is effectively provided by high performance computing clusters.

Appendix

The fluid viscosity defined by the kinetic theory is calculated by the following equation:

$$\mu = 2.6710^{-6}\frac{-6\sqrt{M_{w,i}T}}{\sigma^2\Omega_\mu} \tag{3.11}$$

where, μ is the viscosity $[kg/ms]$, T [K], σ Angstroms and $\Omega_\mu = \Omega_\mu(T^*)$ where, $T^* = \frac{T}{\varepsilon/k_B}$

σ and $\frac{\varepsilon}{k_B}$ provided by user. [16]

The specific heat by using the kinetic theory is:

$$c_{p,i} = \frac{1}{2}\frac{R}{M_{w,i}}(f_i + 2) \tag{3.12}$$

where, f_i is the degrees of freedom for the gas species i.

The thermal conductivity is defined by the kinetic theory as:

$$k = \frac{15}{4}\frac{R}{M_w}\mu[\frac{4}{15}\frac{c_p M_w}{R} + \frac{1}{3}] \tag{3.13}$$

where R is the universal gas constant, M_w is the molecular weight, μ is the materials viscosity, and C_p is the materials heat capacity.

Bibliography

[1] Company profile of osram opto semiconductors. `http://www.osram-os.com/osram_os/EN/`. official website.

[2] K.L. Choy. Chemical vapour deposition of coatings. *Progress in Material Science 48, 57-170*, 2003.

[3] A. K.Hochberg A. Love, S. Middleman. The dynamics of bubblers as vapor delivery systems. *Journal of Crystal Growth 129, 119-133*, 1993.

[4] W. L. Holstein. Performance of gas saturators in the presence of exit stream temperature gradients and implications for chemical vapor deposition saturator design. *Chemical Engineering Science, 0009-2509(94)E0039-S*, 1994.

[5] J.P.Stagg. Reagent concentration measurements in metal organic vapour phase epitaxy (movpe) using an ultrasonic cell. *CHEMTRONICS 3, 44-49*, 1988.

[6] C. Chua D. Bour, Z. Yang. Simple technique for measuring the filled volume of liquid or solid cvd precursor chemicals in bubblers. *Journal of Crystal Growth 310, 2673-2677*, 2008.

[7] N.Tran C.L.Andre, N.El-Zein. Bubbler for constant vapor delivery of a solid chemical. *Journal of Crystal Growth, 298, 168-171*, 2007.

[8] B.D.Nichols C.W.Hirt. Volume of fluid (vof) method for the dynamics of free boundaries. *Journal of Computational Physics 39, 201-225*, 1981.

[9] W. Malalasekera H.K. Versteeg. *An Introduction to Computational Fluid Dynamics; The Finite Volume Method*. Longman Scientific and Technical, 605 Third Avenue, New York, NY 10158, 1995.

[10] I. Harter L. Raynal. Studies of gas-liquid flow through reactors internals using vof simulations. *Proceedings of the 5th International Conference on Gas-Liquid and Gas-Liquid-Solid Reactor Engineering*, 2001.

[11] C.Zemach I.U. Brackbill, D.B.Koethe. A continuum method for modeling surface tension. *Journal of Computational Physics 100, 335-354*, 1992.

[12] G.Arampatzis D. Asimakopoulos, V.Ligerou. *Mass transfer (in Greek)*. Papasotiriou Publ., Athens, 2008.

[13] M.Bayat A.Hassanvand, S.H.Hashemabadi. Evaluation in gasoline evaporation during the tank splash loading by cfd techniques. *International Communications in Heat and Mass Transfer 37 907-913*, 2011.

[14] R.Banerjee. Turbulent conjugate heat and mass transfer from the surface of a binary mixture of ethanol/iso-octane in a countercurrent stratified two phase flow system. *International Journal of Heat and Mass Transfer 51 5958-5974*, 2008.

[15] J.L. Ferzieger and M. Peric. *Computational Methods for Fluid Dynamics*. Springer-Verlag, Heidelberg, 1996.

[16] Ansys. Ansys fluent theory guide, 2011.

[17] Akzonobel hpmo. `http://www.akzonobel.com/hpmo/products/trimethylgallium/`. Viscosity of liquid TMG.

[18] Company profile of aspen. `http://www.aspentech.com/`. official website.

[19] V.G. Vasil'ev E.N. Karataev E.N. Dregich I.A. Feshchenko B.V. Lebedev, N.N. Smirnova. Thermodynamic characteristics of highly pure trimethylgallium within the range 0-330k. *Journal of Crystal Growth*, 1988.

[20] J.P.O'Connell B.E.Poling, J.M.Prausnitz. *The Properties of Gases and Liquids, fifth ed.* McGraw-Hill, New York, 2000.

[21] J. Mitrovic. Josef stefan and his evaporation-diffusion tube-the stefan diffusion problem. *Chemical Engineering Science*, 2012.

[22] M.Kay. *Practical Hydraulics*. Taylor and Francis, 1998.

[23] J.R.Grace R.Clift and M.E.Weber. *Bubbles,Drops and Particles*. Academic Press, New York, San Francisco, London, 1978.

[24] Pegasus cluster. `http://febui.chemeng.ntua.gr/pegasus.htm`. Pegasus: A high-performance cluster, NTUA, Chemical Engineering School.